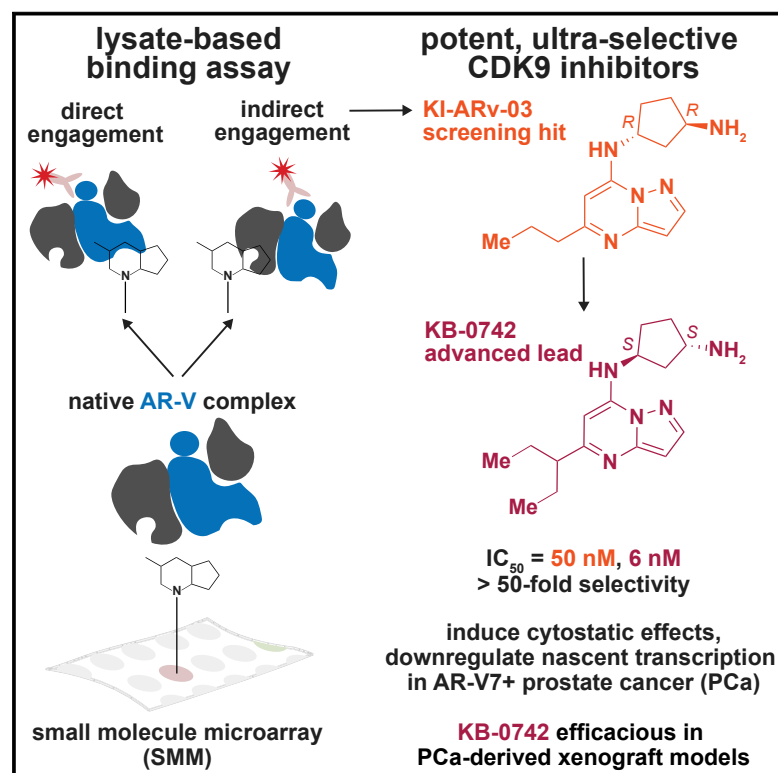# Cell Chemical Biology

Modulating Androgen Receptor-Driven Transcription in Prostate Cancer with Selective CDK9 Inhibitors

Graphical Abstract

Authors

André Richters, Shelby K. Doyle, David B. Freeman, ..., Charles Y. Lin, Marius S. Pop, Angela N. Koehler

Correspondence

koehler@mit.edu

In Brief

In the pursuit of hormone receptor modulators in prostate cancer, a potent, ultraselective CDK9 inhibitor is discovered. This study describes the most selective inhibitors of CDK9 known to date and provides compelling preclinical *in vitro* and *in vivo* support for CDK9 as a therapeutic target.

Highlights

- KI-ARv-03 reduces AR protein levels and AR-driven transcription

- KI-ARv-03 is deduced to be a potent, ultraselective inhibitor of CDK9

- Optimization led to the orally bioavailable and selective CDK9 inhibitor KB-0742

- KB-0742 displays potent anti-tumor activity in cancer models *in vitro* and *in vivo*

CellPress

Cell Chemical Biology

CellPress
OPEN ACCESS

Article

Modulating Androgen Receptor-Driven Transcription in Prostate Cancer with Selective CDK9 Inhibitors

André Richters,[1,2,3,14] Shelby K. Doyle,[1,2,3,4,14] David B. Freeman,[5] Christina Lee,[5] Becky S. Leifer,[1,2,3]
Sajjeev Jagannathan,[6] Florian Kabinger,[1,2,3] Jošt Vrabič Koren,[6] Nicholas B. Struntz,[1,2,3] Julie Urgiles,[1,7] Ryan A. Stagg,[1,8]
Brice H. Curtin,[1,2,3] Deep Chatterjee,[9] Sebastian Mathea,[9] Peter J. Mikochik,[5] Tamara D. Hopkins,[5] Hua Gao,[5]
Jonathan Branch,[10] Hong Xin,[10] Lori Westover,[10] Gilles C. Bignan,[10] Brent A. Rupnow,[10] Kristen L. Karlin,[6]
Calla M. Olson,[6] Thomas F. Westbrook,[6] Joseph Vacca,[5] Chris M. Wilfong,[5] B. Wesley Trotter,[5] Douglas C. Saffran,[5]
Norbert Bischofberger,[5] Stefan Knapp,[9] Joshua W. Russo,[11] Ian Hickson,[10,12] James R. Bischoff,[10] Marco M. Gottardis,[10]
Steven P. Balk,[11] Charles Y. Lin,[5,6,13] Marius S. Pop,[5] and Angela N. Koehler[1,2,3,4,15,*]

[1]David H. Koch Institute for Integrative Cancer Research, Massachusetts Institute of Technology, Cambridge, MA 02142, USA
[2]MIT Center for Precision Cancer Medicine, Massachusetts Institute of Technology, Cambridge, MA 02142, USA
[3]Broad Institute of MIT and Harvard, Cambridge, MA 02142, USA
[4]Department of Biological Engineering, Massachusetts Institute of Technology, Cambridge, MA 02139, USA
[5]Kronos Bio, Inc., Cambridge, MA 02139, USA
[6]Therapeutic Innovation Center, Department of Biochemistry and Molecular Biology, Baylor College of Medicine, Houston, TX 77030, USA
[7]Harvard-MIT Health Sciences and Technology, Boston, MA 02115, USA
[8]Department of Biology, Boston University, Boston, MA 02215, USA
[9]Goethe-Universität Frankfurt, 60438 Frankfurt am Main, Germany
[10]Janssen Research & Development, LLC, Spring House, PA, USA
[11]Beth Israel Deaconess Medical Center, Harvard Medical School, Boston, MA 02215, USA
[12]Cancer Research UK Newcastle Drug Discovery Unit, Translational and Clinical Research Institute, Newcastle University, Newcastle upon Tyne NE2 4HH, UK
[13]Department of Molecular and Human Genetics, Baylor College of Medicine, Houston, TX, USA
[14]These authors contributed equally
[15]Lead Contact
*Correspondence: koehler@mit.edu
https://doi.org/10.1016/j.chembiol.2020.10.001

SUMMARY

Castration-resistant prostate cancers (CRPCs) lose sensitivity to androgen-deprivation therapies but frequently remain dependent on oncogenic transcription driven by the androgen receptor (AR) and its splice variants. To discover modulators of AR-variant activity, we used a lysate-based small-molecule microarray assay and identified KI-ARv-03 as an AR-variant complex binder that reduces AR-driven transcription and proliferation in prostate cancer cells. We deduced KI-ARv-03 to be a potent, selective inhibitor of CDK9, an important cofactor for AR, MYC, and other oncogenic transcription factors. Further optimization resulted in KB-0742, an orally bioavailable, selective CDK9 inhibitor with potent anti-tumor activity in CRPC models. In 22Rv1 cells, KB-0742 rapidly downregulates nascent transcription, preferentially depleting short half-life transcripts and AR-driven oncogenic programs. In vivo, oral administration of KB-0742 significantly reduced tumor growth in CRPC, supporting CDK9 inhibition as a promising therapeutic strategy to target AR dependence in CRPC.

INTRODUCTION

Prostate cancer is a hormone-driven disease that will affect one in nine men (Siegel et al., 2019). Central to prostate cancer therapeutics is the inhibition of androgen receptor (AR)-driven oncogenic signaling and downstream transcription. Treatments intended to ablate AR activity (chemical or surgical castration) and impede AR-controlled gene expression programs by preventing ligand-dependent receptor activation. For instance, AR antagonists such as enzalutamide are potent binders of the ligand-binding domain (LBD) that efficiently block androgen binding and AR activation in prostate cancers (Hoffman-Censits and Kelly, 2013; Tran et al., 2009). However, most patients will develop resistance to standard androgen-deprivation therapies (ADTs) and progress to the stage of castration-resistant prostate cancer (CRPC) due to a variety of mechanisms that appear to reactivate the AR pathway (Chandrasekar et al., 2015; Karantanos et al., 2013).

The emergent expression of alternative splice variants of AR (AR-Vs) lacking the LBD represent one prominent mechanism
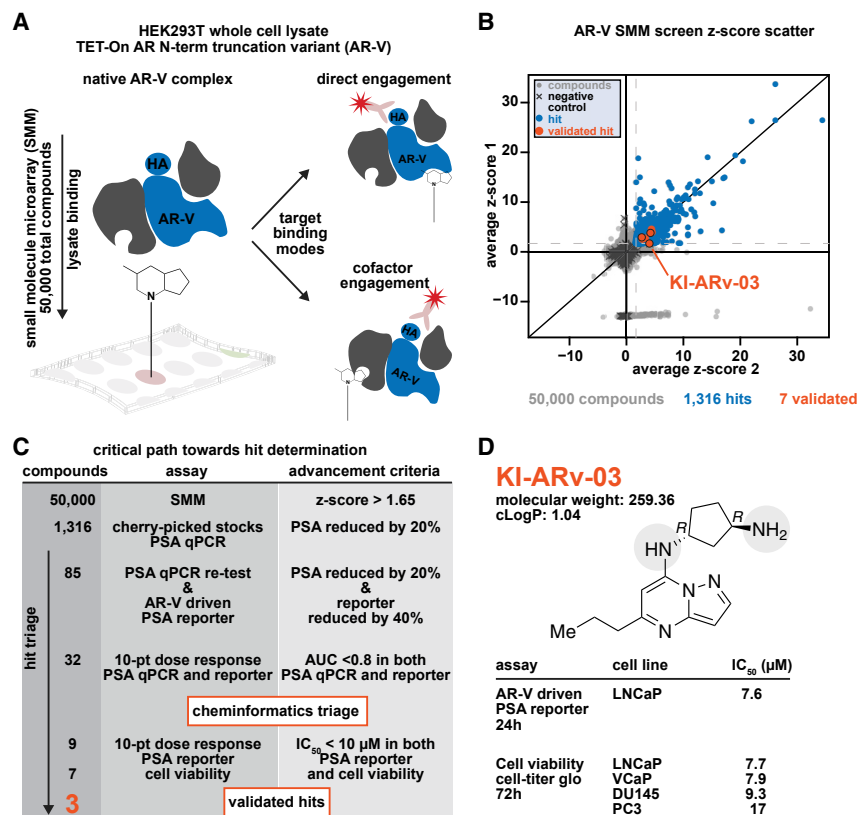
Figure 1. Discovery of KI-ARv-03 as Modulator of AR Transcriptional Output

(A) SMM assay principle. Small-molecule compounds are immobilized on a glass surface and a subset is capable of binding the desired target either directly or indirectly via an essential interaction partner.

(B) Scatterplot of high-throughput SMM screening data of 50,000 compounds against an N-terminal HA-tagged AR-ΔLBD truncate. Assay positives, blue; validated compounds, orange.

(C) Critical path to hit determination leads to three validated probe candidates after multiple rounds of secondary screening.

(D) Chemical structure of **KI-ARv-03**. Intrinsic nucleophiles for SMM surface immobilization are highlighted in gray.

See also Figures S1 and S2.

Importantly, SMMs are able to identify binders of target protein complexes in a physiologically relevant lysate context. As opposed to pure-protein screening, this has two distinct advantages. First, proteins such as AR-Vs that are unstructured in solution can be screened as a complex, where they are more likely to adopt a defined and context-specific structure. Second, by screening the AR-V protein-protein complex in its entirety, druggable cofactors can also be identified as candidate hit targets and interrogated for their potential to indirectly disrupt AR-V activity.

Here, we leveraged the SMM approach to screen an N-terminal truncate of AR in a lysate-based format to discover small molecules capable of engaging the AR-V native complex. We prosecuted putative binders of AR variant complexes through a series of downstream AR-focused functional assays to identify a lead probe candidate and subsequently unmasked the AR interactome member cyclin-dependent kinase 9 (CDK9) as the true molecular target of our inhibitor.

RESULTS

Discovery of KI-ARv-03 as a Modulator of AR Transcriptional Output

We used SMMs to screen whole-cell lysates containing an N-terminal hemagglutinin (HA)-tagged AR-ΔLBD truncate (AR-V) overexpressed in HEK293T cells against a set of 50,000 immobilized compounds (Figure 1A). This library included fragments, lead-like molecules, and precompetitive drug-like structures as well as an overrepresentation of rapamycin, an FKBP12 binder that is unrelated to AR and AR signaling, to represent a null distribution (Figures S1A and S1B). The screen yielded 1,316 putative AR-V and interactome binders with an average robust Z score of ≥1.96 across four replicates (Figure 1B).

Using a medium-throughput qRT-PCR assay, we evaluated the ability of these hits to reduce prostate-specific antigen (PSA; encoded by *KLK3*) transcript levels in the AR-dependent LNCaP prostate cancer cell line (Figures 1S and S1C). This
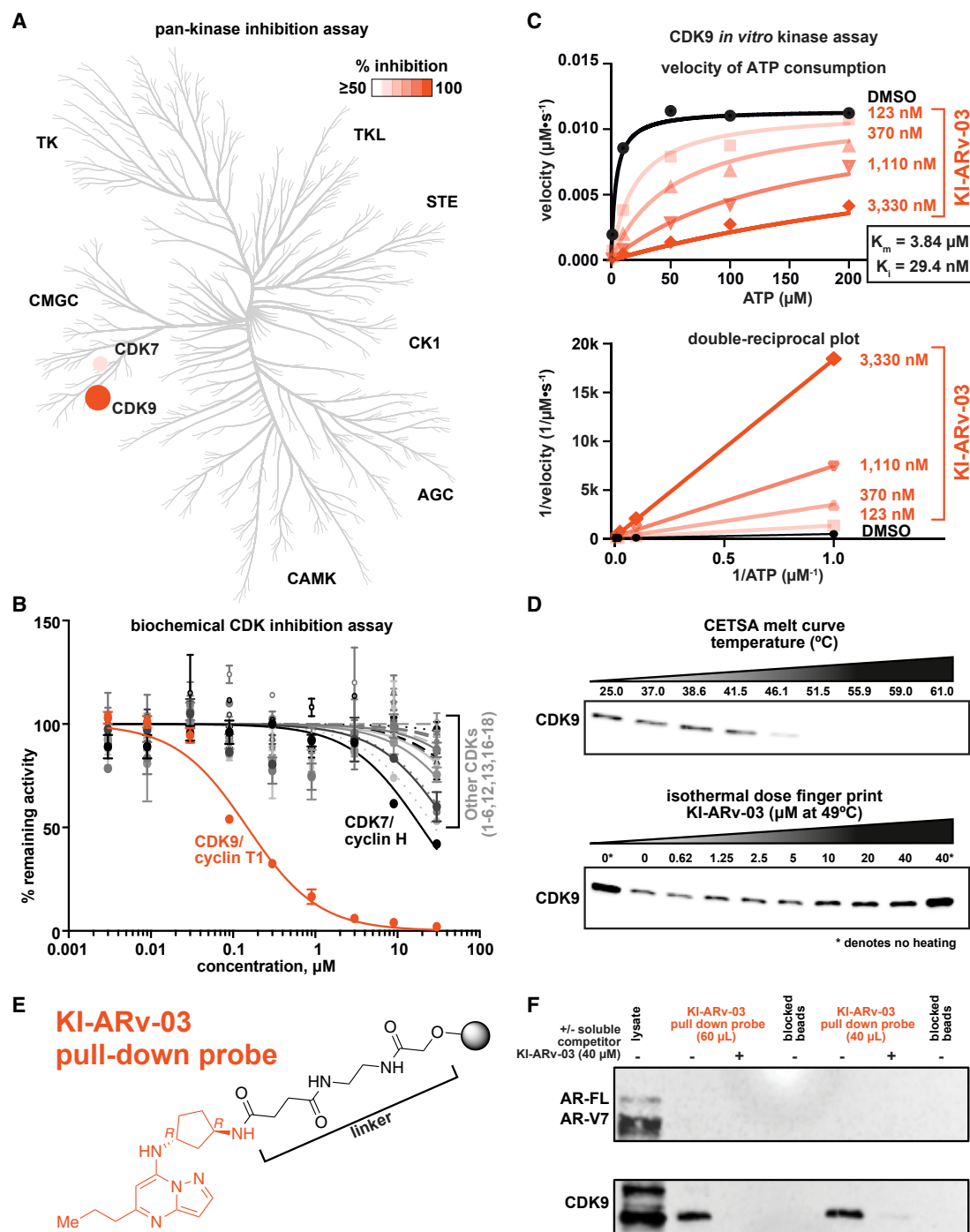
of acquired ADT resistance. These AR-Vs produce constitutively active forms of AR against which there are no known inhibitory small molecules (Hörnberg et al., 2011). The most frequent AR-V, AR-V7, is highly expressed in patients that experience resistance to ADTs (Antonarakis et al., 2014; Sharp et al., 2019) and has been shown to heterodimerize with AR to repress growth suppressor genes in CRPC (Cato et al., 2019). Importantly, these tumors are dependent on both AR-V7 and full-length AR (AR-FL), and still express oncogenic AR-driven gene expression programs. Therefore, agents that inhibit the function of AR and its splice variants independent of the LBD or indirectly via modulating shared interactome members may be efficacious for CRPC patients.

In the absence of their LBDs, AR-Vs are largely unstructured and considered classically undruggable (McEwan, 2012). Thus, innovative approaches are required to identify small molecules that can bind to and modulate the activity of AR-V complexes in cells. Small-molecule microarrays (SMMs) are a robust and scalable screening platform for protein–small-molecule binders in which small molecules are displayed on a glass slide and protein binders are fluorescently detected (Bradner et al., 2006; Vegas et al., 2008). Previously, this approach has led to the identification of small-molecule binders across a broad range of target classes, including transcription factors such as ETV1 and MAX (Pop et al., 2014a; Struntz et al., 2019), epigenetic regulators like histone deacetylases (Boskovic et al., 2016), secreted proteins like Sonic hedgehog (Stanton et al., 2009), and DNA/RNA targets such as G-quadruplexes (Felsenstein et al., 2016).

Cell Chemical Biology
Article

Figure 2. KI-ARv-03 Engages and Selectively Inhibits CDK9 in Biochemical and Cellular Assays

(A) Phylogenetic tree representation of molecular kinase targets of **KI-ARv-03** profiled against 413 kinases (Eurofins KinaseProfiler). Circles indicate >50% inhibition upon treatment with 10 μM **KI-ARv-03**.

(B) Dose-response curves for biochemical inhibition of a focused CDK panel (Eurofins KinaseProfiler, ATP at K_m) after **KI-ARv-03** treatment (n = 2 technical replicates, error bars represent mean ± SD).

(C) Michaelis-Menten and Lineweaver-Burk plots of the kinetic study of CDK9 treatment with **KI-ARv-03** in the presence of various ATP concentrations (HotSpot Kinase Assay, Reaction Biology Corp.).

(D) Melt curve of CDK9 protein levels in the soluble fraction in intact 22Rv1 cells exposed to different temperatures (25°C–61°C) prior to lysis visualized by immunoblotting (top). CETSA CDK9 isothermal fingerprint of the soluble fraction of intact 22Rv1 cells following 1 h **KI-ARv-03** dosing treatment (0–40 μM) at 49°C (bottom).

(legend continued on next page)

marker was chosen as a proxy for AR activity because its transcription is primarily regulated by AR through androgen-responsive elements present in the promoter region of the *KLK3* gene body. PSA is also utilized in prostate cancer patients as a blood-based biomarker for monitoring disease progression (Gelmini et al., 2003b). LNCaP cells were starved of androgens in charcoal-stripped serum medium (low androgen levels) and AR activation and PSA expression were subsequently induced with synthetic androgen R1881 (Bonne and Raynaud, 1975; Gelmini et al., 2003a). Eighty-five small molecules at 10 μM decreased PSA levels by 20% or more after 24 h treatment compared with the R1881-induced condition (Figure S1C).

We evaluated these molecules in a mouse mammary tumor virus (MMTV)-driven stable luciferase reporter gene assay in LNCaP cells with a doxycycline-inducible element for exogenous expression of AR-V. Androgen-starved cells (suppressed AR-FL activity) were treated with R1881 and concomitantly induced for AR-V expression using doxycycline and cotreated with DMSO or our putative binders for 24 h. We prioritized 32 compounds that both attenuated R1881-induced PSA expression in LNCaP by >20% and inhibited the AR-V-driven luciferase signal in the reporter cell line by at least 40% (Figure S1C). These were then subjected to 10-point dose evaluation using qPCR for PSA and luciferase reporter, yielding nine compounds that exhibited dose-dependent reduction of PSA transcripts and AR-responsive promoter occupancy (Figure S1D). We then assessed favorable chemotype characteristics such as drug likeliness, cLogP, and synthetic accessibility for compounds that scored with area under the curve (AUC) values of <0.80 in both assays and prioritized seven compounds for further study. Three probe candidates were selected based on their single-digit micromolar half-maximal inhibitory concentration (IC_{50}) values in both the MMTV-driven reporter gene assay and the viability assay for AR-positive cell lines (Figures S1D and S2A).

KI-ARv-03 was selected based on reasonable physicochemical properties and its single-digit micromolar inhibitory activity in both the reporter assay (IC_{50} = 7.6 μM) and the viability assays for AR-dependent over AR-independent prostate cancer cell lines (VCaP and LNCaP versus DU145 and PC3, Figures 1D, S1D, and S2A). In VCaP-16, an enzalutamide-resistant prostate cancer cell line expressing increased levels of AR-V7, treatment with 5 μM **KI-ARv-03** dramatically decreased *KLK3* transcript levels (Figure S2B). The decrease in *KLK3* expression coincided with decreases in AR-V7 transcript and protein, while AR-FL transcript and protein levels remained unchanged (Figures S2C and S2D). Similar decreases in AR-V7 protein levels were observed in the castration-resistant cell line 22Rv1 in response to **KI-ARv-03** treatment (Figure S2D). Unlike VCaP-16, the decreases in AR-V7 protein levels in 22Rv1 did not coincide with decreases in *KLK3* transcript, which could be due to the higher level of AR-V7 protein expression seen in 22Rv1 compared with VCaP-16. In summary, we identify **KI-ARv-03** as a putative interactor with the

AR-V7 complex in lysates that has attractive drug-like properties and the ability to potently downregulate AR and AR-V7-dependent transcription in CRPC models.

Kinase Profiling and Cellular Target Engagement Identify CDK9 as the Molecular Target of KI-ARv-03

We next sought to determine the molecular target of our lead candidate **KI-ARv-03** using *in vitro* and cell-based techniques. Structurally, **KI-ARv-03** features a pyrazolopyrimidine core with multiple potential H-bond-accepting groups that is substituted with molecular entities incorporating H-bond-donating amino groups. The overarching composition incorporates molecular features that are typically found in ATP-competitive kinase inhibitors (Traxler et al., 1997; Traxler and Furet, 1999). Therefore, we performed *in vitro* kinase selectivity profiling against a panel of 413 kinases (Table S1) using 10 μM **KI-ARv-03** and ATP concentrations at or within 15 μM of the apparent K_m of each kinase to determine if kinase inhibition might give rise to the observed AR-related cellular effects.

Surprisingly, we observed selective reduction of enzymatic activity of the transcriptional CDKs CDK9 and CDK7 to 7% and 47% compared with DMSO treatment (Figure 2A). Given the high structural conservation within the kinome and particularly the CMGC family of kinases, we evaluated **KI-ARv-03** against 13 CDKs at 10-point dose to assess selectivity within the CDK family of kinases (Figure 2B). The compound selectively inhibited CDK9 (IC_{50} = 0.15 μM at 45 μM ATP) over all other tested CDKs with a minimum of 130-fold selectivity. Kinetic studies and Michaelis-Menten analysis for CDK9 inhibition by **KI-ARv-03** in the presence of varying ATP concentrations illustrate that the apparent K_m is increased when inhibitor concentration is increased (Figures 2C and S3A). Lineweaver-Burk plotting illustrates increased slopes for the linear fit with increasing concentration of **KI-ARv-03** and all linear regressions converging on the y axis (Figure 2C). Overall these data suggest CDK9 as the molecular target of **KI-ARv-03** and confirm an ATP competitive mode of CDK9/cyclin T1 inhibition.

Next, we investigated the ability of **KI-ARv-03** to directly engage CDK9 in live cells by employing a cellular thermal shift assay (CETSA) in AR-V7-positive 22Rv1 prostate cancer cells (Martinez Molina et al., 2013). A small molecule that binds a cellular target protein generally leads to a protein-ligand complex with increased heat stability over the unbound protein, which increases the soluble amount of target protein following heat shock. Protein populations of CDK9, AR-FL, and splice variants in 22Rv1 cells become undetectable in the soluble fraction by immunoblotting after heat shock at temperatures between 46°C and 51°C (Figures 2D and S3B). Isothermal dose-response fingerprints were generated in subsequent CETSA studies at 49°C using increasing concentrations of **KI-ARv-03** (0–40 μM, 1 h treatment). At 10 μM compound concentration we observed significant stabilization of CDK9 as illustrated by increased protein levels compared with DMSO treatment. We did not observe any significant stabilization of AR-FL or AR-V7 at any applied

---

(E) **KI-ARv-03** (orange) covalently bound to solid support (black, Affi-Gel 10 beads) via the compound's terminal primary amine using NHS-facilitated amide formation.

(F) Target engagement studies in 22Rv1 cell lysates using **KI-ARv-03** displayed on agarose beads demonstrating reversible engagement of CDK9.

See also Table S1 and Figure S3.

Cell Chemical Biology
Article

CellPress
OPEN ACCESS

dose (Figure S3B), supporting our hypothesis that **KI-ARv-03** does not directly engage AR species but rather affects AR levels through impaired CDK9 enzymatic activity.

To evaluate whether **KI-ARv-03** engages CDK9 only, CDK9 and AR independently, or any complex of these, we utilized a bead-based approach for target engagement from 22Rv1 cell lysates (and others, Figures 2E, 2F, and S3C–S3F). We used NHS-activated agarose beads to attach **KI-ARv-03** (Figures 2E and S3F) to a solid support through its terminal primary amine in the same way that our SMM surface chemistry captured and displayed the compound in the lysate-based screening (Figure S3C). We used high-salt RIPA buffer for 22Rv1 cell lysis to break up any protein-protein and protein-DNA/RNA interactions and engage single targets only. We observed robust and specific enrichment of the most abundant isoform of CDK9 (43 kDa) from 22Rv1 cell lysate by **KI-ARv-03** compared with ethanolamine-blocked control beads (Figure 2F). CDK9 engagement was reversible as demonstrated by soluble competition experiments using 40 μM free **KI-ARv-03**. There was no engagement of AR-FL or its truncate versions. Using mild MIPP lysis buffer, which maintains protein-protein and protein-DNA/RNA interactions in lysates (Pop et al., 2014b), we observed engagement of both isoforms of CDK9 compared with blocked beads (Figure S3D). This interaction was reversible upon competition with free **KI-ARv-03** as well as structurally unrelated ATP-competitive CDK9 reference inhibitors NVP-2 (Barsanti et al., 2011), BAY-1143572 (atuveciclib) (Lücking et al., 2017), and MC180295 (Zhang et al., 2018) (Figure S3E, Table S2).

In addition, we observed engagement of both AR-FL and truncate versions such as AR-V7. These interactions were irreversible, as neither free **KI-ARv-03** nor any of the structurally unrelated CDK9 inhibitors was able to attenuate binding of engaged AR protein. Furthermore, coimmunoprecipitation experiments on AR-FL and AR-V7 from 22Rv1 cells under mild lysis conditions did not demonstrate a stable protein-protein interaction with CDK9 in our hands in the presence or absence of **KI-ARv-03** (Figure S3G). Therefore, we speculate that AR and CDK9 do interact transiently and directly in the regulation of Ser81 in the N terminus of AR (Koryakina et al., 2014). The enrichment for AR-FL and AR-V7 observed with **KI-ARv-03** beads is most likely CDK9 independent, either through transient interactions between immobilized **KI-ARv-03** and the N terminus of AR or between immobilized **KI-ARv-03** and AR-containing complexes.

CDK9 Regulates AR Stability and Is Required for Downstream AR Target Gene Expression

Among known AR interactome members of potential therapeutic advantage are regulatory kinases. CDK9, for instance, is a serine/threonine kinase from the CDK family, of which multiple members are involved in the regulation of either cell-cycle progression or gene transcription (Lim and Kaldis, 2013; Malumbres, 2014). CDK9 extends the AR half-life and activity through its N-terminal phosphorylation (Ser81). Unphosphorylated AR is exported from the nucleus, where it is ubiquitinated and degraded by the proteasome (Koryakina et al., 2014). Inhibition of CDK9 therefore may offer an indirect route for AR modulation in CRPC. **KI-ARv-03** treatment (5 μM) leads to reduction of both AR-FL and AR-V7 phosphorylation at Ser81 after 4 h, concurrent

with loss of protein levels for both AR species starting at 6 h of treatment (Figure S4C). AR protein and phosphorylation levels are rescued upon cotreatment with the proteasome inhibitor MG132 (Figure S4D).

CDK9 and cyclin T1 form the positive transcription elongation factor b (P-TEFb), which facilitates phosphorylation of Ser2 of the C-terminal domain of RNA polymerase II (RNA Pol II), ultimately initiating transcriptional elongation (Hirose and Ohkuma, 2007). P-TEFb inhibition enables selective downregulation of oncogenes by decreasing RNA Pol II Ser2 phosphorylation, resulting in universal RNA Pol II stalling that disproportionately downregulates sites of heavy transcriptional recruitment and transcriptional cooperativity at superenhancers within transcriptional condensates or insulated environments (Bradner et al., 2017; Cho et al., 2018; Guo et al., 2019; Jonkers and Lis, 2015; Lovén et al., 2013; Weintraub et al., 2017). Consequently, transcriptional CDK inhibitors, including those that preferentially inhibit CDK9, have shown strong potential as therapeutic agents owing to their ability to selectively downregulate oncogenic transcription programs and target tumors addicted to transcription factors such as AR or MYC (Huang et al., 2014). We demonstrate that treatment of 22Rv1 cells with **KI-ARv-03** (5 μM) leads to significant reduction of RNA Pol II phosphorylation after 6 and 24 h (Figures S4C and S4D). Translational inhibition with cycloheximide (20 μg/mL) depletes AR levels, similar to CDK9 inhibition. Proteasome inhibition with MG132 (10 μM) rescues AR protein levels, but cotreatment with **KI-ARv-03** does not decrease AR pS81 levels. Together, these data suggest downregulation of AR transcription as the key mechanism for **KI-ARv-03**-mediated effects on AR protein levels.

Transcriptional CDK inhibitors have been explored clinically but have had limited success. It is unclear whether these limitations are due to small therapeutic index, lack of selectivity, or unfavorable pharmacology. Notably, most clinical transcriptional CDK inhibitors have hit multiple CDKs. CDK9 has been shown to be a promising and druggable target in oncology for attenuating oncogenic transcription for a variety of indications (Blake et al., 2019; Brisard et al., 2018; Franco et al., 2018; Hashiguchi et al., 2019; Mitra et al., 2016; Morales and Giordano, 2016; Wang et al., 2019). However, as CDK9 also plays a global role in transcription, a sufficient therapeutic index for clinical benefit has not yet been demonstrated. **KI-ARv-03** treatment (5 μM) leads to robust and sustained impact on AR transcript levels in 22Rv1 cells compared with treatments with the structurally unrelated CDK9 inhibitor NVP-2 or a separate RNA Pol II inhibition mechanism using THZ1, a covalent inhibitor of CDKs 7, 12, and 13 that elicits transcriptional defects by inhibition of superenhancer-associated gene expression (Kwiatkowski et al., 2014; Olson et al., 2019; Zhang et al., 2016) (Figure S5A).

Prior clinical investigation of transcriptional CDK inhibitors has been confounded by off-target interactions with other kinases, especially other CDKs that play important roles in transcription and the cell cycle. Due to the high structural conservation of the ATP-binding cleft in kinases it is challenging to accomplish selective inhibition for single CDKs across the family of CDKs as well as across the kinome. We demonstrated that **KI-ARv-03** is a selective CDK9 inhibitor that ultimately modulates AR and AR-V7-dependent transcription *in vitro*.
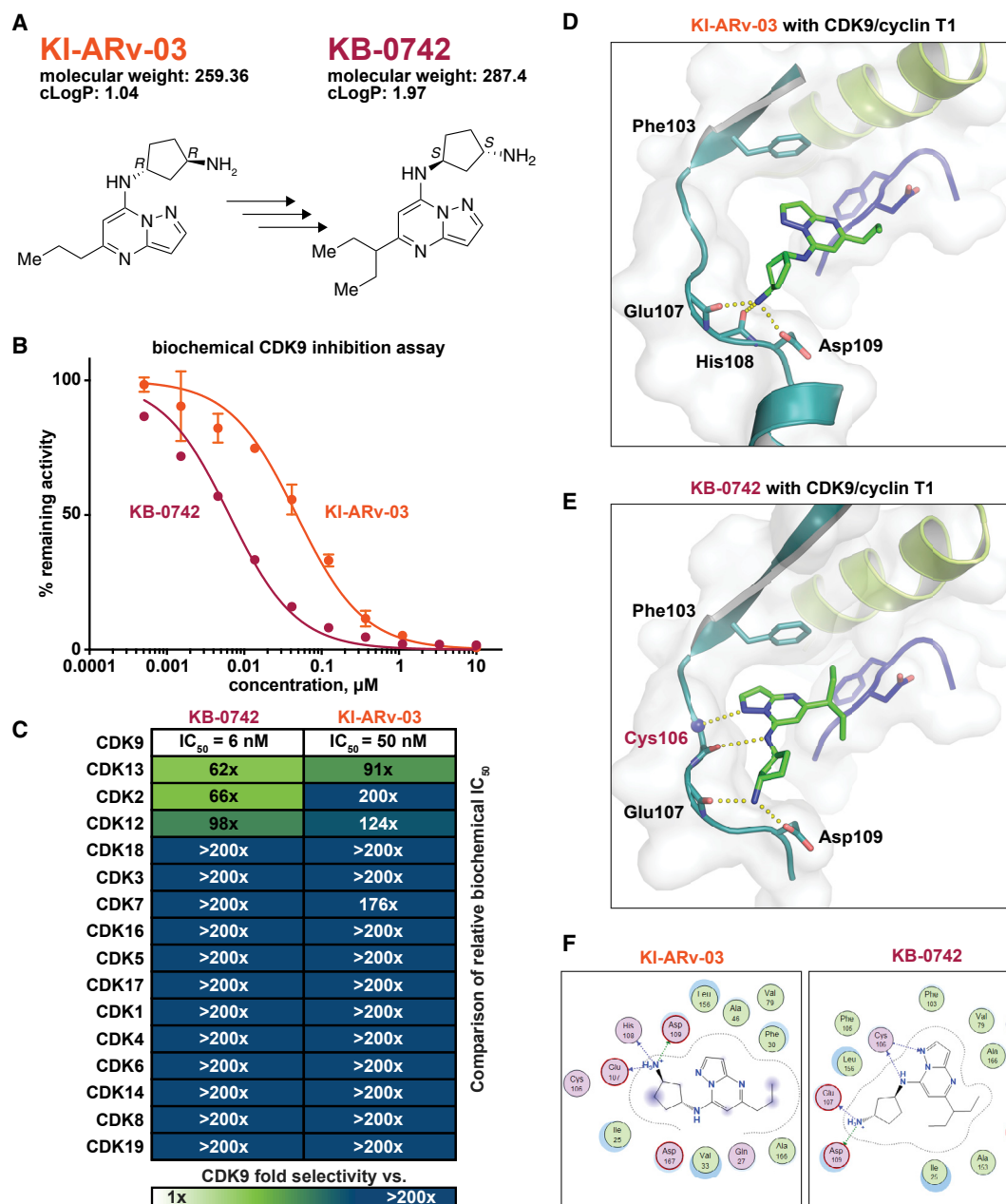
Figure 3. KB-0742 Is a Potent and Selective CDK9 Inhibitor

(A) Chemical structures of parent compound **KI-ARv-03** and optimized molecule **KB-0742**.

(B) Dose-response curves for biochemical CDK9/cyclin T1 inhibition (at 10 μM ATP concentration; HotSpot Kinase Assay, Reaction Biology Corp.) after treatment with **KI-ARv-03** and **KB-0742** (n = 2 technical replicates, error bars represent mean ± SD).

(C) Heatmap representation of biochemical inhibition of CDK family members by **KI-ARv-03** and **KB-0742** (HotSpot Kinase Assay).

(D and E) Molecular docking of (D) **KI-ARv-03** (green sticks) and (E) **KB-0742** (green sticks) into the ATP-binding cleft of CDK9 (PDB: 3MY1). Hinge, teal; DFG motif, blue; helix αC, lime; hydrogen bonds, yellow spheres.

(F) Molecular interaction map of **KI-ARv-03** (left) and **KB-0742** (right) with key amino acids for ligand binding within the binding cleft of CDK9.

Structure-Based Considerations and Medicinal Chemistry Optimization Yield the Potent and Selective CDK9 Inhibitor KB-0742

Given the remarkable up-front selectivity of **KI-ARv-03**, we aimed to optimize its potency and simultaneously retain its selectivity for CDK9. To better understand structure-activity rela-

tionships and molecular recognition, we undertook crystallization efforts using recombinant CDK9/cyclin T1 and **KI-ARv-03**. Due to the low resolution of the resulting hexagonal crystals we were not able to generate a high-quality complex structure. Therefore, we utilized molecular modeling to assess the binding mode of **KI-ARv-03** in complex with CDK9/cyclin T1 (Figures 3D

Cell Chemical Biology
Article

CellPress
OPEN ACCESS

and 3F). Our modeling suggests that the compound binds to the catalytic cleft of CDK9 in a type I fashion, establishing H-bond interactions through the terminal primary amine with the hinge backbone amides of His108 and Glu107, as well as an ionic interaction with the side chain of Asp109. The *R,R* configuration of the cyclopentane-1,3-diamine prevents the establishment of additional H bonds through the pyrazolopyrimidine core of **KI-ARv-03**. Consecutive compound optimization efforts resulted in the identification of the more potent CDK9 inhibitor **KB-0742** (CDK9/cyclin T1 inhibition IC_{50} = 6 nM at 10 μM ATP, Figures 3A and 3B).

KB-0742 incorporates beneficial features to increase potency that include: (1) a branched 3-pentane extension of the propane alkyl chain that increases Van der Waals interactions with the glycine-rich loop and (2) inverted stereochemistry of the cyclopentane-1,3-diamine, which preserves the terminal primary amine interactions with Asp109 and Glu107 while also enabling two H-bond interactions between the backbone amide of Cys106 (NH and CO) and the bridging secondary amine and pyrazolopyrimidine core of **KB-0742** (Figures 3E and 3F). The compound was subjected to kinase selectivity profiling and found to be selective for CDK9/cyclin T1 with >50-fold selectivity over all CDKs profiled and >100-fold selectivity against cell-cycle CDKs (CDK1-6) in the panel (Figure 3C).

KI-ARv-03 and KB-0742 Show Cytostatic Effects in Prostate Cancer and Leukemia Cell Lines

Next, we performed growth rate inhibition (GR) studies with our CDK9 inhibitors in 22Rv1 prostate cancer cells over time and at 72 h of treatment compared with the known CDK9 inhibitors NVP-2, BAY-1143572, and AZD4573 (Cidado et al., 2020) (Figures 4A, S4A, and S4B). These studies reflect the 10-fold *in vitro* improvement of CDK9 inhibitory potency of **KI-ARv-03** versus **KB-0742**, which translated into an 18-fold improvement of antiproliferative activity in 22Rv1 cells (GR_{50} = 3.26 μM versus 0.18 μM). Monitoring induction of apoptosis by caspase-3/7 activation, we observed a similar trend, with **KI-ARv-03** only moderately increasing apoptotic cell counts at high doses (10 and 3 μM), while no apoptotic cells were produced at submicromolar doses (Figure 4B). **KB-0742** follows the same trend, with stronger induction of apoptosis at higher doses and additionally little induction at doses as low as 0.3 μM. Analogous behavior was observed for BAY-1143572, while NVP-2 and AZD4573 drove 22Rv1 cells into massive events of apoptosis even at double-digit nanomolar concentrations, with NVP-2 generally inducing stronger apoptotic signals than AZD4573.

Beyond its implication in transcriptional regulation of AR activity in prostate cancer and general transcriptional regulation, CDK9 is a key molecular target in transcriptionally driven diseases such as acute myeloid leukemia (AML) (Boffo et al., 2018; Lee and Zeidner, 2019; Tibes and Bogenberger, 2019). Therefore, we examined growth inhibition and apoptosis-inducing properties of our compounds in MV-4-11 AML cells. We observed the same growth inhibition rates but more prevalent induction of apoptosis for **KI-ARv-03**, **KB-0742**, and BAY-1143572 (Figures 4C and 4D). NVP-2 and AZD4573 demonstrated GR_{50} values in the single-digit nanomolar range and a substantial caspase-3/7 activation even at doses as low as 0.001 μM. Overall, we find that MV-4-11 AML cells are slightly

more susceptible to CDK9 inhibition than 22Rv1 prostate cancer cells.

Immunoblotting studies in 22Rv1 cells after 6 h treatment with **KI-ARv-03** and **KB-0742** demonstrate significant reduction of downstream phosphorylation of RNA Pol II at Ser2 and Ser7 (Figure 4E), even at low doses (0.1–0.5 μM), while only **KB-0742** diminishes phosphorylation at Ser5 and only at the highest applied dose (2.5 μM). Total RNA Pol II and CDK9 protein levels were not affected by treatment with any inhibitor utilized in this study. To assess our CDK9 inhibitors with respect to their effects on transcription factors regulated by CDK9 activity, we performed a time-course study (Figure 4F) with fixed concentrations of **KI-ARv-03** (5 μM) and **KB-0742** (1 μM). Global AR-FL and AR-V protein levels are significantly reduced starting at 6 h treatment time, which is accompanied by the reduction of phospho-AR levels (Ser81). Complete depletion of AR levels is obtained after 16 h of treatment for both compounds. This result is in line with previous findings demonstrating that lack of AR phosphorylation at Ser81 entails nuclear export of AR, its subsequent ubiquitination, and proteasomal degradation (Koryakina et al., 2014). From our observations, however, this AR effect appears to be proteasome independent and is also observed with CDK9 inhibitors of unrelated structural scaffolds (e.g., NVP-2, Figures S4C and S4D), suggesting that **KI-ARv-03** and **KB-0742** achieve this effect primarily through CDK9-mediated transcriptional regulation of the AR locus versus CDK9-mediated regulation of the AR gene product.

KI-ARv-03 and KB-0742 Block Nascent Transcription and Downregulate Oncogenic Prostate Cancer Gene Expression Programs

CDK9 inhibition or degradation has been shown to globally downregulate nascent transcription (Olson et al., 2018; Winter et al., 2017). To place inhibition of AR-driven transcriptional programs in the overall context of global transcriptional response, we performed nascent transcriptional profiling using SLAM-seq (thiol(SH)-linked alkylation for the metabolic sequencing of RNA) (Muhar et al., 2018). SLAM-seq measures the incorporation of a metabolic uracil analog that is chemically converted and detected as a mutation upon sequencing. As a metabolic labeling assay, it enables a more direct measurement of nascent transcription than traditional RNA sequencing, which samples cellular mRNA composition. We performed SLAM-seq at concentrations (**KI-ARv-03** 4 μM and **KB-0742** 1.2 μM) sufficient to reduce RNA Pol II Ser2 phosphorylation and induce growth arrest and sampled cells at early time points (2, 4, and 8 h) to capture more immediate and direct changes in gene expression that occur prior to gross changes in cellular phenotype.

Across the 8 h time course, we observe a steady increase in nascent mRNA metabolic labeling under DMSO conditions that is blunted by either **KI-ARv-03** or **KB-0742** treatment (Figures 5A and S5B). By 8 h, 95% of high-confidence actively transcribed genes show downregulated nascent transcription in treatments versus DMSO, consistent with a global role for CDK9. Based on nascent transcription levels, samples tend to cluster by time point and then by treatment, with little difference between **KI-ARv-03** and **KB-0742** (Figure S5C). The strongest divergence between DMSO and CDK9 inhibition is observed at 8 h. Across genes, changes in nascent transcription correlate
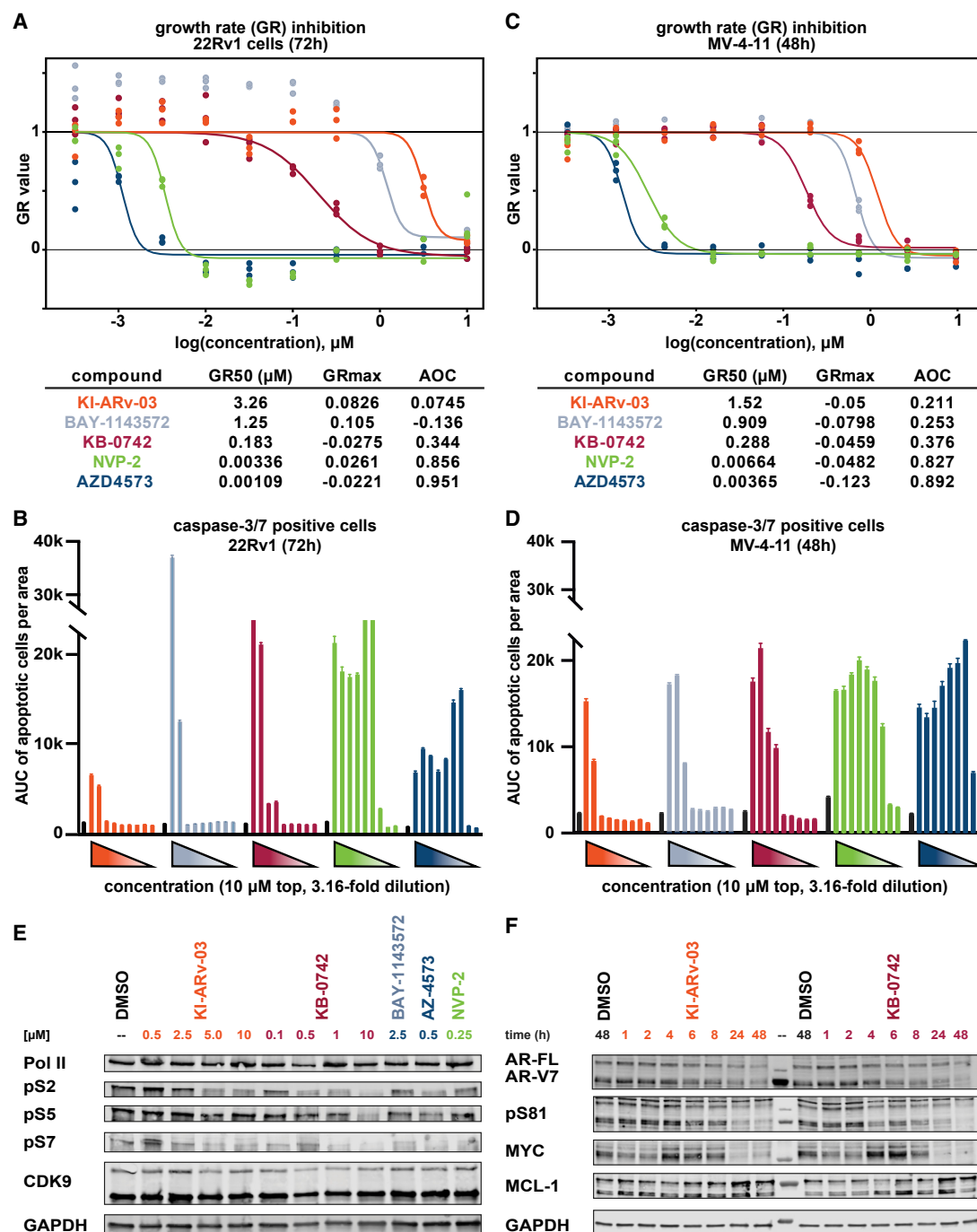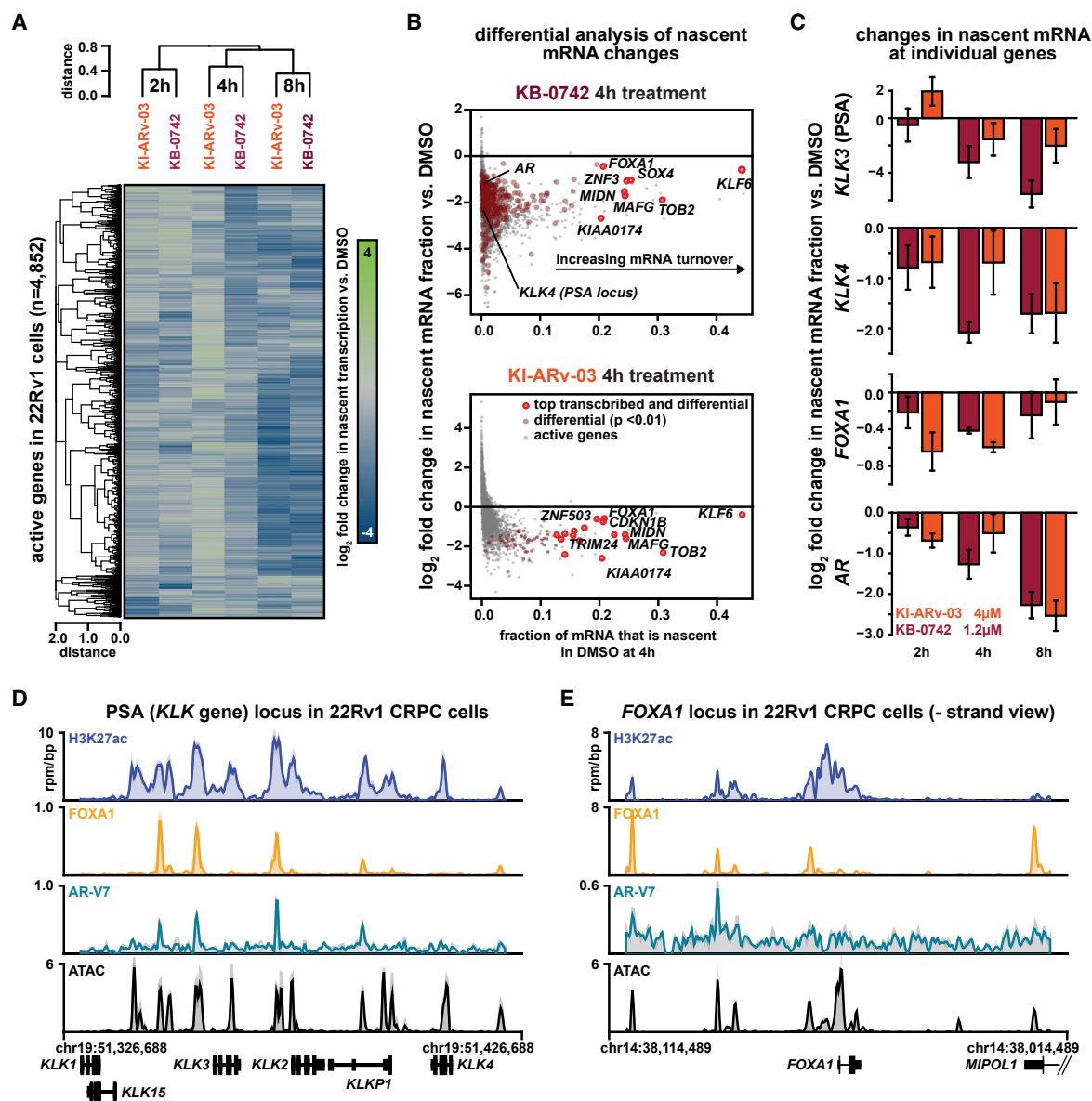
Figure 4. KI-ARv-03 and KB-0742 Induce Apoptosis in Prostate Cancer and Leukemia Cell Lines

(A and C) Dose-response curves and growth rate inhibition of (A) 22Rv1 prostate cancer cells and (C) MV-4-11 AML cells after treatment with **KI-ARv-03**, **KB-0742**, and reference CDK9 inhibitors AZD4573, BAY-1143572, and NVP-2 (0–40 μM, n = 3 technical replicates).

(B and D) Induction of apoptosis in (B) 22Rv1 and (D) MV-4-11 cells monitored as a function of caspase 3/7 activation after treatment with **KI-ARv-03**, **KB-0742**, and reference CDK9 inhibitors (0–10 μM, n = 3 technical replicates).

(E) Immunoblot of dose-response study of CDK9 and (phospho)-RNA Pol II levels in 22Rv1 after 6 h treatment with **KI-ARv-03**, **KB-0742** and reference CDK9 inhibitors.

(F) Immunoblot of time course of CDK9 downstream target and interactome protein levels in 22Rv1 in response to treatment with **KI-ARv-03** (5 μM) and **KB-0742** (1 μM).

See also Figures S3 and S4.

Figure 5. KI-ARv-03 and KB-0742 Block Nascent Transcription and Downregulate Oncogenic Prostate Cancer Gene Expression Programs

(A) Heatmap of log$_2$ fold change in nascent mRNA labeling fraction in treatment versus DMSO across time points and treatments. Rows representing all active genes (n = 4,852) and columns representing treatments are hierarchically clustered.

(B) Scatterplots comparing changes in nascent mRNA levels upon drug treatment with nascent mRNA labeling fraction under DMSO conditions at 4 h. The y axis shows log$_2$ fold change in nascent mRNA labeling fraction versus DMSO. The x axis shows nascent mRNA labeling fraction in DMSO.

(C) Bar plots showing log$_2$ fold change in nascent mRNA labeling fraction versus DMSO across the treatment time course for **KI-ARv-03** (orange) and **KB-0742** (dark red). Selected genes relevant to prostate cancer are shown. Error bars represent mean ± SEM.

(D and E) Gene tracks showing signal for H3K27ac ChIP-seq (blue), FOXA1 ChIPmentation (light orange), AR-V7 ChIP-exo (light blue), and ATAC-seq at (D) the PSA locus and (E) the FOXA1 locus. The y axis shows signal in units of reads per million per base pairs (rpm/bp). Multiple replicates are overlaid with the mean signal (thick line). The x axis shows position along the genome. Genes are depicted as boxes below the tracks.

See also Figure S5.

well between **KI-ARv-03** and **KB-0742** (Figure S5D). These data suggest that selective CDK9 inhibition blunts nascent RNA Pol II transcription and that at respective dose/time points, **KI-ARv-03** and **KB-0742** elicit similar transcriptional responses.

Differential analysis identifies a subset of genes in which CDK9 inhibition has a more pronounced impact (Figures 5B and 5C). Comparing highly with lowly transcribed genes, we do not

observe differential effects on mRNA synthesis rates (Figures 5B and 5C). However, changes in mature mRNA levels for the top transcribed differential genes versus other differential genes demonstrate distinct selective effects on mature mRNA levels (p = 0.0007 and p = 0.0001) for **KB-0742** and **KI-ARv-03**, respectively (Figure S5E), suggesting that these genes are more influenced by CDK9 inhibition. Although we observe downregulation
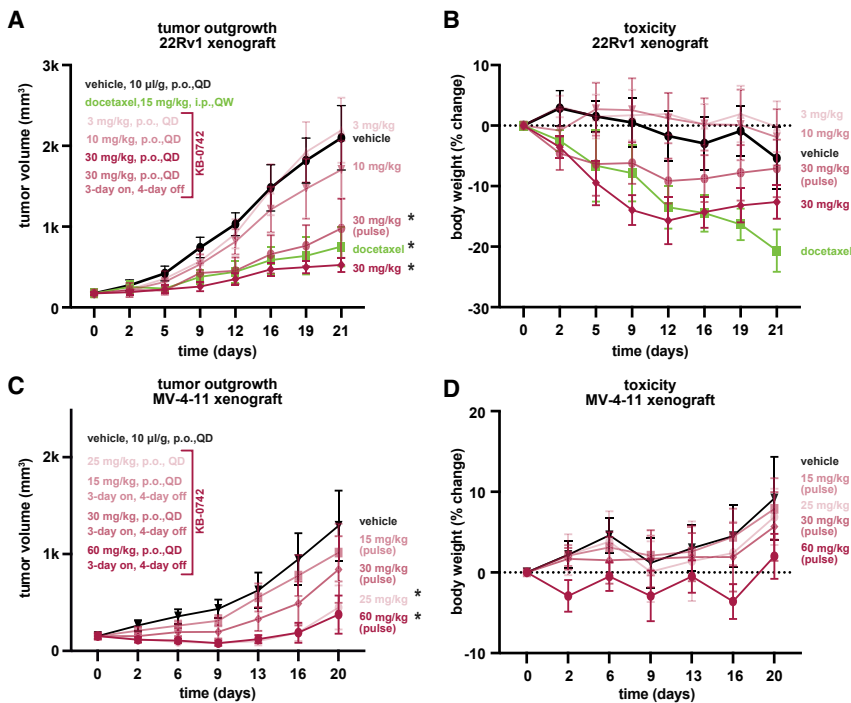
Figure 6. KB-0742 Reduces Tumor Burden in CRPC and AML Xenograft Models

(A and B) (A) Tumor growth inhibition curves and (B) percentage body weight changes for treatment groups (n = 10, vehicle, docetaxel, **KB-0742**) in a male CB17-SCID mouse bearing 22Rv1 human prostate cancer CDX model.

(C and D) (C) Tumor growth inhibition curves and (D) percentage body weight changes for treatment groups (n = 10, vehicle, **KB-0742**) in a female BALB/c nude mouse bearing MV-4-11 human AML CDX model.

Data points represent group mean body weight. Error bars represent mean ± SEM. *p < 0.001, significant effect compared with vehicle. See also Figure S6 and Tables S3–S6.

of AR and PSA locus genes (*KLK* family genes), we also note that these genes are not highly transcribed under control (DMSO) conditions. Instead we find significant downregulation of several highly transcribed transcription factors, including *KLF6*, *FOXA1*, *SOX4*, *MAFG*, and *ZNF3*. SOX4 and FOXA1 serve as lineage-defining transcription factors in prostate cancer (Adams et al., 2019; Parolia et al., 2019; Scharer et al., 2009). MAFG is associated with chemoresistance in other cancers (Vera-Puente et al., 2018). Interestingly, KLF6 is a tumor suppressor that is recurrently mutated in prostate cancer (at least 25% of all tumors) (Liu et al., 2012). These data are consistent with a preferential effect of CDK9 inhibition on highly transcribed genes, which often include master transcription factors associated with tumor or lineage identity.

Inspection of key prostate cancer loci, including PSA (*KLK3*) and *FOXA1*, shows regions of hyperacetylated and accessible chromatin (H3K27ac chromatin immunoprecipitation sequencing [ChIP-seq] and assay for transposase-accessible chromatin sequencing [ATAC-seq]) bound by both FOXA1 and AR-V7 (Figures 5D and 5E). Interestingly, across the 8 h time course, lineage transcription factors such as FOXA1 show more immediate-early downregulation that is followed by later downregulation of AR and PSA genes (*KLK3* and *KLK4*) (Figure 5C). From these data we conclude that CDK9 inhibition suppresses nascent RNA Pol II transcription and collapses AR-driven transcription programs and their upstream master regulators (e.g., FOXA1).

KB-0742 Exhibits Efficacy in Prostate Cancer and AML-Derived Xenograft Models

To assess the therapeutic potential of **KB-0742** we performed *in vivo* efficacy studies using subcutaneous 22Rv1 human prostate cancer cell line-derived xenograft (CDX) models in male

CB17-SCID mice (Figures 6A and 6B, Tables S3 and S4). Subsequent to tumor establishment, mice (n = 10) were treated with vehicle (by mouth [p.o.], once a day [QD]), standard docetaxel chemotherapy (intraperitoneally, 15 mg/kg, once a week), or escalating doses of **KB-0742** (p.o., 3, 10, and 30 mg/kg, QD) over 21 days. **KB-0742** does not lead to any tumor or body weight reduction at 3 and 10 mg/kg daily dosing compared with vehicle treatment. At 30 mg/kg, we observe stagnating tumor burden reflected as 82% (p = 0.000003) tumor growth inhibition (TGI), which is superior to standard docetaxel treatment (TGI = 70%, p = 0.000002). We observe body weight loss in the first week of treatment with **KB-0742**, which then stabilizes at 15% overall body weight loss over the course of treatment. Body weight loss was minimized to 7.5% by applying high-dose **KB-0742** on a scheduled treatment regimen (30 mg/kg, 3 days on/4 days off) but tumor growth reduction was less pronounced here (TGI = 58%, p < 0.00005). These studies demonstrate that **KB-0742** is well tolerated even at high dose, while significantly reducing tumor burden in 22Rv1-driven CDX models.

In addition, we evaluated **KB-0742** in a subcutaneous MV-4-11-driven human AML CDX model with adjusted treatment regimen (Figures 6C and 6D, Tables S5 and S6). **KB-0742** treatment was well tolerated across all groups (n = 10) with applied treatment strategies spanning vehicle (p.o., QD), **KB-0742** (p.o., 25 mg/kg, QD) as well as 3 days on/4 days off QD treatments using escalating doses of **KB-0742** (p.o., 15, 30, and 60 mg/kg). We did not observe any significant body weight changes over the course of the 20 day study (Figure 6D). Daily treatment with 25 mg/kg **KB-0742** leads to substantial reduction in tumor volume, which is reflected in 74% TGI (p < 0.00002). Solely high-dose cyclic dosing of **KB-0742** (60 mg/kg, 3 days on/4 days off QD) led to more substantial tumor volume reduction (TGI = 81%, p < 0.00001). Cyclic treatment at half (30 mg/kg) and quarter (15 mg/kg) **KB-0742** doses resulted in 40% and 24% reduction of tumor burden, respectively. In conclusion, our xenograft studies demonstrate that **KB-0742** treatment is well tolerated *in vivo* at doses of at least 25–30 mg/kg daily, at which significant reduction of tumor burden across 22Rv1 and MV-4-11 CDX models was accomplished.

Cell Chemical Biology
Article

CellPress
OPEN ACCESS

DISCUSSION

Here we sought to identify small-molecule modulators of AR-V activity as a means to overcome resistance to ADT in CRPC. We took advantage of the unbiased and context-based SMM binding platform to identify **KI-ARv-03**, an inhibitor of the AR-V cofactor CDK9. **KI-ARv-03** inhibits CDK9 in cells and leads to downregulation of AR-driven transcription and AR protein phosphorylation and abundance. Interestingly, as a low-molecular-weight screening hit, **KI-ARv-03** displayed remarkable up-front selectivity versus other kinases and in particular other CDKs. In our experience, hits from *in vitro* kinase screens often require significant medicinal chemistry optimization and structural elaboration to achieve selectivity. Optimization of **KI-ARv-03** into **KB-0742** increased shape complementarity with the CDK9 ATP-binding pocket without significant increase in molecular weight or at the expense of selectivity, resulting in an ultraselective and single-digit nanomolar potent CDK9 inhibitor. We suspect that the up-front selectivity observed for **KI-ARv-03** may be attributed to the SMM platform, which screened for binding in a more native lysate environment that maintained context-specific structure of the AR-V/CDK9 complex. These findings suggest that the SMM may be particularly advantageous for targets residing in large complexes that are difficult to reconstitute *in vitro*.

CDK9 is a core component of the P-TEFb transcription elongation complex and is required for all active transcription (Olson et al., 2018; Rahl et al., 2010; Winter et al., 2017). We and others have previously shown that targeting core members of the transcriptional complex can have surprisingly selective effects on gene expression, especially on highly transcribed short-half-life genes (Erb et al., 2017; Jaeger et al., 2020; Kwiatkowski et al., 2014; Lovén et al., 2013; Sharifnia et al., 2019; Winter et al., 2017). In 22Rv1 cells, treatment with either **KI-ARv-03** or **KB-0742** results in global downregulation of nascent transcription and, in particular, at highly turned over mRNAs encoding lineage-specific transcription factors. In AML and CRPC cell line xenograft models, oral administration of **KB-0742** is well tolerated and able to significantly inhibit tumor growth.

CRPC, like many other cancers, exhibits evidence of transcriptional addiction (in this case due to AR-driven transcription) (Schweizer and Yu, 2015). There is an open clinical question as to whether transcriptional inhibitors can exploit this vulnerability with acceptable toxicity profiles. Currently, several transcriptional CDK inhibitors, including CDK9-preferring inhibitors, are either in clinical trials or in late-stage preclinical development (Bisi et al., 2017; Cidado et al., 2020; Clark et al., 2017; Goh et al., 2012; Hu et al., 2019; Kawakami et al., 2019; Kim et al., 2017; Lücking et al., 2017). Many of these drugs have activity against multiple CDKs, making it difficult to fully assess the specific contribution of CDK9 inhibition to efficacy. Our data suggest that selective CDK9 inhibition is an attractive therapeutic strategy for transcriptionally addicted tumor types such as CRPC and that the orally bioavailable lead **KB-0742** is a promising candidate for clinical development.

SIGNIFICANCE

Castration-resistant prostate cancers (CRPCs) are insensitive to classical androgen-deprivation therapies but commonly dependent on androgen receptor (AR)-driven oncogenic transcriptional programs. One eminent resistance mechanism is the expression of constitutively active AR splice variants (AR-Vs) lacking the ligand-binding domain typically addressed by anti-androgen inhibitors. AR-Vs are mostly unstructured in solution and do not feature druggable binding pockets; therefore, targeting druggable AR interactome members constitutes a suitable and promising path to abrogate AR activity. We have successfully applied our unbiased small-molecule microarray platform in a context-specific approach to identify direct modulators of an N-terminal truncate of AR and its interactome members in lysate-based screenings. We identified KI-ARv-03 and developed KB-0742, which both modulate AR transcriptional programs by reducing AR and AR-V protein levels through selective inhibition of its cofactor CDK9, an essential member of the transcriptional elongation machinery. Moreover, CDK9 facilitates the N-terminal phosphorylation of AR and thereby regulates its half-life as well as downstream AR target gene expression, which nominates CDK9 as a suitable and druggable therapeutic target in CRPC. Many of the clinically explored transcriptional CDK inhibitors target multiple CDKs and have had limited success. KB-0742 is a remarkably selective CDK9 inhibitor that leads to global downregulation of nascent transcription and AR-driven prostate cancer gene expression programs and displays *in vivo* efficacy in CRPC- and AML-derived xenograft models. Therefore, our selective and orally bioavailable CDK9 inhibitor KB-0742 is a promising candidate for further clinical development in CRPC and other transcriptionally addicted cancers.

STAR★METHODS

Detailed methods are provided in the online version of this paper and include the following:

- KEY RESOURCES TABLE
- RESOURCE AVAILABILITY
  - Lead Contact
  - Materials Availability
  - Data and Code Availability
- EXPERIMENTAL MODEL AND SUBJECT DETAILS
  - Animal Studies
  - Cell Lines
- METHOD DETAILS
  - Expression Vector for HA-Tagged Androgen Receptor N-terminal Truncate
  - SMM Screening of HA-Tagged AR N-terminal Truncate
  - RT-qPCR for PSA in LNCaP Cells
  - Luciferase Reporter Gene Assay
  - Cell Viability Assays
  - Lead Evaluation in Cellular CRPC Models
  - *In Vitro* Kinase Activity Assays
  - Compound-Anchored Target Engagement
  - Cellular Thermal Shift Assay (CETSA)
  - Thermal Shift Assays (TSA)
  - Immunoblotting
  - Growth Rate Inhibition Studies

- ○ Thiol(SH)-Linked Alkylation for the Metabolic Sequencing of RNA (SLAM seq)
- ○ Chromatin Immunoprecipitation (ChIP)
- ○ Omni Assay for Transposase-Accessible Chromatin (Omni-ATAC)
- ○ Library Preparations
- ○ 22Rv1 Human Prostate Cancer Xenograft Model in Male CB17-SCID Mice
- ○ MV-4-11 Human AML Xenograft in Female BALB/c Nude Mice
- ○ Chemical Synthesis
- ● QUANTIFICATION AND STATISTICAL ANALYSIS

SUPPLEMENTAL INFORMATION

Supplemental Information can be found online at https://doi.org/10.1016/j.chembiol.2020.10.001.

REFERENCES

Adams, E.J., Karthaus, W.R., Hoover, E., Liu, D., Gruet, A., Zhang, Z., Cho, H., DiLoreto, R., Chhangawala, S., Liu, Y., et al. (2019). FOXA1 mutations alter pioneering activity, differentiation and prostate cancer phenotypes. Nature *571*, 408–412.

Antonarakis, E.S., Lu, C., Wang, H., Luber, B., Nakazawa, M., Roeser, J.C., Chen, Y., Mohammad, T.A., Chen, Y., Fedor, H.L., et al. (2014). AR-V7 and resistance to enzalutamide and abiraterone in prostate cancer. N. Engl. J. Med. *371*, 1028–1038.

Barsanti, P., Hu, C., Jin, J., Keyes, R., Kucejko, R., Lin, X., Pan, Y., Pfister, K., Sendzik, M., and Sutton, J. (2011). Pyridine and pyrazine derivatives as protein kinase modulators and their preparation and use for the treatment of CDK9-mediated diseases. PCT Int. Appl. 2011, WO 2010-EP60984; WO 2011012661 A1. SciFinder Scholar.

Baumli, S., Endicott, J.A., and Johnson, L.N. (2010). Halogen bonds form the basis for selective P-TEFb inhibition by DRB. Chem. Biol. *17*, 931–936.

Baumli, S., Lolli, G., Lowe, E.D., Troiani, S., Rusconi, L., Bullock, A.N., Debreczeni, J.E., Knapp, S., and Johnson, L.N. (2008). The structure of P-TEFb (CDK9/cyclin T1), its complex with flavopiridol and regulation by phosphorylation. EMBO J. *27*, 1907–1918.

Bisi, J.E., Sorrentino, J.A., Jordan, J.L., Darr, D.D., Roberts, P.J., Tavares, F.X., and Strum, J.C. (2017). Preclinical development of G1T38: a novel, potent and selective inhibitor of cyclin dependent kinases 4/6 for use as an oral antineoplastic in patients with CDK4/6 sensitive tumors. Oncotarget *8*, 42343–42358.

Blake, D.R., Vaseva, A.V., Hodge, R.G., Kline, M.P., Gilbert, T.S.K., Tyagi, V., Huang, D., Whiten, G.C., Larson, J.E., Wang, X., et al. (2019). Application of a MYC degradation screen identifies sensitivity to CDK9 inhibitors in KRAS-mutant pancreatic cancer. Sci. Signal. *12*, eaav7259.

Boffo, S., Damato, A., Alfano, L., and Giordano, A. (2018). CDK9 inhibitors in acute myeloid leukemia. J. Exp. Clin. Cancer Res. *37*, 36.

Bonne, C., and Raynaud, J.P. (1975). Methyltrienolone, a specific ligand for cellular androgen receptors. Steroids *26*, 227–232.

Boskovic, Z.V., Kemp, M.M., Freedy, A.M., Viswanathan, V.S., Pop, M.S., Fuller, J.H., Martinez, N.M., Figueroa Lazú, S.O., Hong, J.A., Lewis, T.A., et al. (2016). Inhibition of zinc-dependent histone deacetylases with a chemically triggered electrophile. ACS Chem. Biol. *11*, 1844–1851.

Bradner, J.E., Hnisz, D., and Young, R.A. (2017). Transcriptional addiction in cancer. Cell *168*, 629–643.

Bradner, J.E., McPherson, O.M., Mazitschek, R., Barnes-Seeman, D., Shen, J.P., Dhaliwal, J., Stevenson, K.E., Duffner, J.L., Park, S.B., Neuberg, D.S., et al. (2006). A robust small-molecule microarray platform for screening cell lysates. Chem. Biol. *13*, 493–504.

Cell Chemical Biology
Article

CellPress
OPEN ACCESS

Brisard, D., Eckerdt, F., Marsh, L.A., Blyth, G.T., Jain, S., Cristofanilli, M., Horiuchi, D., and Platanias, L.C. (2018). Antineoplastic effects of selective CDK9 inhibition with atuveciclib on cancer stem-like cells in triple-negative breast cancer. Oncotarget 9, 37305–37318.

Buenrostro, J.D., Wu, B., Chang, H.Y., and Greenleaf, W.J. (2015). ATAC-seq: a method for assaying chromatin accessibility genome-wide. Curr. Protoc. Mol. Biol. 109, 21.29.21–21.29.29.

Cato, L., de Tribolet-Hardy, J., Lee, I., Rottenberg, J.T., Coleman, I., Melchers, D., Houtman, R., Xiao, T., Li, W., Uo, T., et al. (2019). ARv7 represses tumor-suppressor genes in castration-resistant prostate cancer. Cancer Cell 35, 401–413.e406.

Chandrasekar, T., Yang, J.C., Gao, A.C., and Evans, C.P. (2015). Mechanisms of resistance in castration-resistant prostate cancer (CRPC). Transl. Androl. Urol. 4, 365–380.

Cho, W.-K., Spille, J.-H., Hecht, M., Lee, C., Li, C., Grube, V., and Cisse, I.I. (2018). Mediator and RNA polymerase II clusters associate in transcription-dependent condensates. Science 361, 412–415.

Cidado, J., Boiko, S., Proia, T., Ferguson, D., Criscione, S.W., San Martin, M., Pop-Damkov, P., Su, N., Roamio Franklin, V.N., Sekhar Reddy Chilamakuri, C., et al. (2020). AZD4573 is a highly selective CDK9 inhibitor that suppresses MCL-1 and induces apoptosis in hematologic cancer cells. Clin. Cancer Res. 26, 922–934.

Clark, K., Ainscow, E., Peall, A., Thomson, S., Leishman, A., Elaine, S., Ali, S., Coombes, R., Barrett, A., and Bahl, A.K. (2017). CT7001, a novel orally bio-available CDK7 inhibitor, is highly active in in-vitro and in-vivo models of AML. Blood 130, 2645.

Clemons, P.A., Bodycombe, N.E., Carrinski, H.A., Wilson, J.A., Shamji, A.F., Wagner, B.K., Koehler, A.N., and Schreiber, S.L. (2010). Small molecules of different origins have distinct distributions of structural complexity that correlate with protein-binding profiles. Proc Natl Acad Sci U S A 107, 18787–18792.

Corces, M.R., Trevino, A.E., Hamilton, E.G., Greenside, P.G., Sinnott-Armstrong, N.A., Vesuna, S., Satpathy, A.T., Rubin, A.J., Montine, K.S., Wu, B., et al. (2017). An improved ATAC-seq protocol reduces background and enables interrogation of frozen tissues. Nat. Methods 14, 959–962.

Erb, M.A., Scott, T.G., Li, B.E., Xie, H., Paulk, J., Seo, H.S., Souza, A., Roberts, J.M., Dastjerdi, S., Buckley, D.L., et al. (2017). Transcription control by the ENL YEATS domain in acute leukaemia. Nature 543, 270–274.

Fedorov, O., Niesen, F.H., and Knapp, S. (2012). Kinase inhibitor selectivity profiling using differential scanning fluorimetry. Methods Mol. Biol. 795, 109–118.

Felsenstein, K.M., Saunders, L.B., Simmons, J.K., Leon, E., Calabrese, D.R., Zhang, S., Michalowski, A., Gareiss, P., Mock, B.A., and Schneekloth, J.S. (2016). Small molecule microarrays enable the identification of a selective, quadruplex-binding inhibitor of MYC expression. ACS Chem. Biol. 11, 139–148.

Franco, L.C., Morales, F., Boffo, S., and Giordano, A. (2018). CDK9: a key player in cancer and other diseases. J. Cell. Biochem. 119, 1273–1284.

Gelmini, S., Tricarico, C., Petrone, L., Forti, G., Amorosi, A., Dedola, G.L., Serio, M., Pazzagli, M., and Orlando, C. (2003a). Real-time RT-PCR for the measurement of prostate-specific antigen mRNA expression in benign hyperplasia and adenocarcinoma of prostate. Clin. Chem. Lab. Med. 41, 261.

Gelmini, S., Tricarico, C., Petrone, L., Forti, G., Amorosi, A., Dedola, G.L., Serio, M., Pazzagli, M., and Orlando, C. (2003b). Real-time RT-PCR for the measurement of prostate-specific antigen mRNA expression in benign hyperplasia and adenocarcinoma of prostate. Clin. Chem. Lab. Med. 41, 261–265.

Goh, K.C., Novotny-Diermayr, V., Hart, S., Ong, L.C., Loh, Y.K., Cheong, A., Tan, Y.C., Hu, C., Jayaraman, R., William, A.D., et al. (2012). TG02, a novel oral multi-kinase inhibitor of CDKs, JAK2 and FLT3 with potent anti-leukemic properties. Leukemia 26, 236–243.

Guo, Y.E., Manteiga, J.C., Henninger, J.E., Sabari, B.R., Dall'Agnese, A., Hannett, N.M., Spille, J.-H., Afeyan, L.K., Zamudio, A.V., Shrinivas, K., et al. (2019). Pol II phosphorylation regulates a switch between transcriptional and splicing condensates. Nature 572, 543–548.

Hashiguchi, T., Bruss, N., Best, S., Lam, V., Danilova, O., Paiva, C.J., Wolf, J., Gilbert, E.W., Okada, C.Y., Kaur, P., et al. (2019). Cyclin-dependent kinase-9 is a therapeutic target in MYC-expressing diffuse large B-cell lymphoma. Mol. Cancer Ther. 18, 1520–1532.

Herzog, V.A., Reichholf, B., Neumann, T., Rescheneder, P., Bhat, P., Burkard, T.R., Wlotzka, W., von Haeseler, A., Zuber, J., and Ameres, S.L. (2017). Thiol-linked alkylation of RNA to assess expression dynamics. Nat Methods 14, 1198–1204.

Hirose, Y., and Ohkuma, Y. (2007). Phosphorylation of the C-terminal domain of RNA polymerase II plays central roles in the integrated events of eucaryotic gene expression. J. Biochem. 141, 601–608.

Hoffman-Censits, J., and Kelly, W.K. (2013). Enzalutamide: a novel antiandrogen for patients with castrate-resistant prostate cancer. Clin. Cancer Res. 19, 1335–1339.

Hörnberg, E., Ylitalo, E.B., Crnalic, S., Antti, H., Stattin, P., Widmark, A., Bergh, A., and Wikström, P. (2011). Expression of androgen receptor splice variants in prostate cancer bone metastases is associated with castration-resistance and short survival. PLoS One 6, e19059.

Hu, S., Marineau, J., Hamman, K., Bradley, M., Savinainen, A., Alnemy, S., Rajagopal, N., Orlando, D., Chuaqui, C., and Olson, E. (2019). Abstract 4421: SY-5609, an orally available selective CDK7 inhibitor demonstrates broad anti-tumor activity in vivo. Cancer Res. 79, 4421.

Huang, C.H., Lujambio, A., Zuber, J., Tschaharganeh, D.F., Doran, M.G., Evans, M.J., Kitzing, T., Zhu, N., de Stanchina, E., Sawyers, C.L., et al. (2014). CDK9-mediated transcription elongation is required for MYC addiction in hepatocellular carcinoma. Genes Dev. 28, 1800–1814.

Jaeger, M.G., Schwalb, B., Mackowiak, S.D., Velychko, T., Hanzl, A., Imrichova, H., Brand, M., Agerer, B., Chorn, S., Nabet, B., et al. (2020). Selective Mediator dependence of cell-type-specifying transcription. Nat. Genet. 52, 719–727.

Jafari, R., Almqvist, H., Axelsson, H., Ignatushchenko, M., Lundbäck, T., Nordlund, P., and Martinez Molina, D. (2014). The cellular thermal shift assay for evaluating drug target interactions in cells. Nat. Protoc. 9, 2100–2122.

Jonkers, I., and Lis, J.T. (2015). Getting up to speed with transcription elongation by RNA polymerase II. Nat. Rev. Mol. Cell Biol. 16, 167–177.

Karantanos, T., Corn, P.G., and Thompson, T.C. (2013). Prostate cancer progression after androgen deprivation therapy: mechanisms of castrate resistance and novel therapeutic approaches. Oncogene 32, 5501–5511.

Kawakami, M., Mustachio, L.M., Chen, Y., Chen, Z., Roszik, J., Liu, X., and Dmitrovsky, E. (2019). Abstract 4407: next generation CDK2/9 inhibitor CYC065 triggers anaphase catastrophe in diverse aneuploid cancers and markedly inhibits growth and metastasis. Cancer Res. 79, 4407.

Kim, W., Haws, H., Peterson, P., Whatcott, C.J., Weitman, S., Warner, S.L., Bearss, D.J., and Siddiqui-Jain, A. (2017). Abstract 5133: TP-1287, an oral pro-drug of the cyclin-dependent kinase-9 inhibitor alvocidib. Cancer Res. 77, 5133.

Koryakina, Y., Ta, H.Q., and Gioeli, D. (2014). Androgen receptor phosphorylation: biological context and functional consequences. Endocr. Relat. Cancer 21, T131–T145.

Kwiatkowski, N., Zhang, T., Rahl, P.B., Abraham, B.J., Reddy, J., Ficarro, S.B., Dastur, A., Amzallag, A., Ramaswamy, S., Tesar, B., et al. (2014). Targeting transcription regulation in cancer with a covalent CDK7 inhibitor. Nature 511, 616–620.

Lee, D.J., and Zeidner, J.F. (2019). Cyclin-dependent kinase (CDK) 9 and 4/6 inhibitors in acute myeloid leukemia (AML): a promising therapeutic approach. Expert Opin. Investig. Drugs 28, 989–1001.

Lim, S., and Kaldis, P. (2013). Cdks, cyclins and CKIs: roles beyond cell cycle regulation. Development 140, 3079–3093.

Liu, X., Gomez-Pinillos, A., Loder, C., Carrillo-de Santa Pau, E., Qiao, R., Unger, P.D., Kurek, R., Oddoux, C., Melamed, J., Gallagher, R.E., et al. (2012). KLF6 loss of function in human prostate cancer progression is implicated in resistance to androgen deprivation. Am. J. Pathol. 181, 1007–1016.

Lovén, J., Hoke, H.A., Lin, C.Y., Lau, A., Orlando, D.A., Vakoc, C.R., Bradner, J.E., Lee, T.I., and Young, R.A. (2013). Selective inhibition of tumor oncogenes by disruption of super-enhancers. Cell 153, 320–334.

Lücking, U., Scholz, A., Lienau, P., Siemeister, G., Kosemund, D., Bohlmann, R., Briem, H., Terebesi, I., Meyer, K., Prelle, K., et al. (2017). Identification of atuveciclib (BAY1143572), the first highly selective, clinical PTEFb/CDK9 inhibitor for the treatment of cancer. ChemMedChem 12, 1776–1793.

Malumbres, M. (2014). Cyclin-dependent kinases. Genome Biol. 15, 122.

Martinez Molina, D., Jafari, R., Ignatushchenko, M., Seki, T., Larsson, E.A., Dan, C., Sreekumar, L., Cao, Y., and Nordlund, P. (2013). Monitoring drug target engagement in cells and tissues using the cellular thermal shift assay. Science 341, 84–87.

McEwan, I.J. (2012). Intrinsic disorder in the androgen receptor: identification, characterisation and drugability. Mol. Biosyst. 8, 82–90.

Mitra, P., Yang, R.-M., Sutton, J., Ramsay, R.G., and Gonda, T.J. (2016). CDK9 inhibitors selectively target estrogen receptor-positive breast cancer cells through combined inhibition of MYB and MCL-1 expression. Oncotarget 7, 9069–9083.

Morales, F., and Giordano, A. (2016). Overview of CDK9 as a target in cancer research. Cell Cycle 15, 519–527.

Muhar, M., Ebert, A., Neumann, T., Umkehrer, C., Jude, J., Wieshofer, C., Rescheneder, P., Lipp, J.J., Herzog, V.A., Reichholf, B., et al. (2018). SLAM-seq defines direct gene-regulatory functions of the BRD4-MYC axis. Science 360, 800–805.

Neumann, T., Herzog, V.A., Muhar, M., von Haeseler, A., Zuber, J., Ameres, S.L., and Rescheneder, P. (2019). Quantification of experimentally induced nucleotide conversions in high-throughput sequencing datasets. BMC Bioinformatics 20, 258.

Olson, C.M., Jiang, B., Erb, M.A., Liang, Y., Doctor, Z.M., Zhang, Z., Zhang, T., Kwiatkowski, N., Boukhali, M., Green, J.L., et al. (2018). Pharmacological perturbation of CDK9 using selective CDK9 inhibition or degradation. Nat. Chem. Biol. 14, 163–170.

Olson, C.M., Liang, Y., Leggett, A., Park, W.D., Li, L., Mills, C.E., Elsarrag, S.Z., Ficarro, S.B., Zhang, T., Düster, R., et al. (2019). Development of a selective CDK7 covalent inhibitor reveals predominant cell-cycle phenotype. Cell Chem. Biol. 26, 792–803 e710.

Parolia, A., Cieslik, M., Chu, S.C., Xiao, L., Ouchi, T., Zhang, Y., Wang, X., Vats, P., Cao, X., Pitchiaya, S., et al. (2019). Distinct structural classes of activating FOXA1 alterations in advanced prostate cancer. Nature 571, 413–418.

Pop, M.S., Stransky, N., Garvie, C.W., Theurillat, J.P., Hartman, E.C., Lewis, T.A., Zhong, C., Culyba, E.K., Lin, F., Daniels, D.S., et al. (2014a). A small molecule that binds and inhibits the ETV1 transcription factor oncoprotein. Mol. Cancer Ther. 13, 1492–1502.

Pop, M.S., Wassaf, D., and Koehler, A.N. (2014b). Probing small-molecule microarrays with tagged proteins in cell lysates. Curr. Protoc. Chem. Biol. 6, 209–220.

Rahl, P.B., Lin, C.Y., Seila, A.C., Flynn, R.A., McCuine, S., Burge, C.B., Sharp, P.A., and Young, R.A. (2010). c-Myc regulates transcriptional pause release. Cell 141, 432–445.

Scharer, C.D., McCabe, C.D., Ali-Seyed, M., Berger, M.F., Bulyk, M.L., and Moreno, C.S. (2009). Genome-wide promoter analysis of the SOX4 transcriptional network in prostate cancer cells. Cancer Res. 69, 709–717.

Schmidl, C., Rendeiro, A.F., Sheffield, N.C., and Bock, C. (2015). ChIPmentation: fast, robust, low-input ChIP-seq for histones and transcription factors. Nat. Methods 12, 963–965.

Schweizer, M.T., and Yu, E.Y. (2015). Persistent androgen receptor addiction in castration-resistant prostate cancer. J. Hematol. Oncol. 8, 128.

Sharifnia, T., Wawer, M.J., Chen, T., Huang, Q.Y., Weir, B.A., Sizemore, A., Lawlor, M.A., Goodale, A., Cowley, G.S., Vazquez, F., et al. (2019). Small-molecule targeting of brachyury transcription factor addiction in chordoma. Nat. Med. 25, 292–300.

Sharp, A., Coleman, I., Yuan, W., Sprenger, C., Dolling, D., Rodrigues, D.N., Russo, J.W., Figueiredo, I., Bertan, C., Seed, G., et al. (2019). Androgen receptor splice variant-7 expression emerges with castration resistance in prostate cancer. J. Clin. Invest. 129, 192–208.

Siegel, R.L., Miller, K.D., and Jemal, A. (2019). Cancer statistics, 2019. CA Cancer J. Clin. 69, 7–34.

Stanton, B.Z., Peng, L.F., Maloof, N., Nakai, K., Wang, X., Duffner, J.L., Taveras, K.M., Hyman, J.M., Lee, S.W., Koehler, A.N., et al. (2009). A small molecule that binds Hedgehog and blocks its signaling in human cells. Nat. Chem. Biol. 5, 154–156.

Struntz, N.B., Chen, A., Deutzmann, A., Wilson, R.M., Stefan, E., Evans, H.L., Ramirez, M.A., Liang, T., Caballero, F., Wildschut, M.H.E., et al. (2019). Stabilization of the max homodimer with a small molecule attenuates Myc-driven transcription. Cell Chem. Biol. 26, 711–723 e714.

Tibes, R., and Bogenberger, J.M. (2019). Transcriptional silencing of MCL-1 through cyclin-dependent kinase inhibition in acute myeloid leukemia. Front. Oncol. 9, 1205.

Tran, C., Ouk, S., Clegg, N.J., Chen, Y., Watson, P.A., Arora, V., Wongvipat, J., Smith-Jones, P.M., Yoo, D., Kwon, A., et al. (2009). Development of a second-generation antiandrogen for treatment of advanced prostate cancer. Science 324, 787–790.

Traxler, P., Bold, G., Frei, J., Lang, M., Lydon, N., Mett, H., Buchdunger, E., Meyer, T., Mueller, M., and Furet, P. (1997). Use of a pharmacophore model for the design of EGF-R tyrosine kinase inhibitors: 4-(phenylamino)pyrazolo[3,4-d]pyrimidines. J. Med. Chem. 40, 3601–3616.

Traxler, P., and Furet, P. (1999). Strategies toward the design of novel and selective protein tyrosine kinase inhibitors. Pharmacol. Ther. 82, 195–206.

Vegas, A.J., Fuller, J.H., and Koehler, A.N. (2008). Small-molecule microarrays as tools in ligand discovery. Chem. Soc. Rev. 37, 1385–1387.

Vera-Puente, O., Rodriguez-Antolin, C., Salgado-Figueroa, A., Michalska, P., Pernia, O., Reid, B.M., Rosas, R., Garcia-Guede, A., SacristAn, S., Jimenez, J., et al. (2018). MAFG is a potential therapeutic target to restore chemosensitivity in cisplatin-resistant cancer cells by increasing reactive oxygen species. Transl. Res. 200, 1–17.

Wang, X., Yu, C., Wang, C., Ma, Y., Wang, T., Li, Y., Huang, Z., Zhou, M., Sun, P., Zheng, J., et al. (2019). Novel cyclin-dependent kinase 9 (CDK9) inhibitor with suppression of cancer stemness activity against non-small-cell lung cancer. Eur. J. Med. Chem. 181, 111535.

Weintraub, A.S., Li, C.H., Zamudio, A.V., Sigova, A.A., Hannett, N.M., Day, D.S., Abraham, B.J., Cohen, M.A., Nabet, B., Buckley, D.L., et al. (2017). YY1 is a structural regulator of enhancer-promoter loops. Cell 171, 1573–1579.e1528.

Winter, G.E., Mayer, A., Buckley, D.L., Erb, M.A., Roderick, J.E., Vittori, S., Reyes, J.M., di Iulio, J., Souza, A., Ott, C.J., et al. (2017). BET bromodomain proteins function as master transcription elongation factors independent of CDK9 recruitment. Mol. Cell 67, 5–18 e19.

Zhang, H., Pandey, S., Travers, M., Sun, H., Morton, G., Madzo, J., Chung, W., Khowsathit, J., Perez-Leal, O., Barrero, C.A., et al. (2018). Targeting CDK9 reactivates epigenetically silenced genes in cancer. Cell 175, 1244–1258.e26.

Zhang, T., Kwiatkowski, N., Olson, C.M., Dixon-Clarke, S.E., Abraham, B.J., Greifenberg, A.K., Ficarro, S.B., Elkins, J.M., Liang, Y., Hannett, N.M., et al. (2016). Covalent targeting of remote cysteine residues to develop CDK12 and CDK13 inhibitors. Nat. Chem. Biol. 12, 876–884.

STAR★METHODS

KEY RESOURCES TABLE

REAGENT or RESOURCE	SOURCE	IDENTIFIER
Antibodies		
Mouse monoclonal anti-HA.11 (clone 16B12)	Covance	Cat#MMS-101R-1000, RRID:AB_291262
Goat polyclonal Cy3-conjugated anti-mouse IgG	Millipore	Cat#AP124C, RRID:AB_11213281
Mouse monoclonal anti-c-Myc (9E10)	Santa Cruz Biotechnology	Cat#sc-40, RRID:AB_627268
Rat monoclonal anti-RNA Pol II subunit B1 (phospho-CTD Ser-2) (clone 3E10)	Millipore	Cat#04-1571, RRID:AB_11212363
Rat monoclonal anti-RNA Pol II subunit B1 (phospho-CTD Ser-5) (clone 3E8)	Millipore	Cat#04-1572, RRID:AB_10615822
Rat monoclonal anti-RNA Pol II subunit B1 (phospho-CTD Ser-7) (clone 4E12)	Millipore	Cat# 04-1570-I, RRID:AB_2801298
Mouse monoclonal anti-Pol II (F-12)	Santa Cruz Biotechnology	Cat#sc-55492, RRID:AB_630203
Rabbit polyclonal to RNA Pol II CTD repeat YSPTSPS (phospho S2)	Abcam	Cat #ab5095, RRID:AB_304749)
Mouse monoclonal anti-AR (441)	Santa Cruz Biotechnology	Cat#sc-7305, RRID:AB_626671
Rabbit polyclonal anti-AR (N-20)	Santa Cruz Biotechnology	Cat#sc-816, RRID:AB_1563391
Rabbit monoclonal anti-AR-V7 (clone EPR15656)	Abcam	Cat#ab198394, RRID:AB_2716436
Rabbit monoclonal anti AR-V7 (clone RM7)	RevMAb Biosciences	Cat#31-1109-00
Rabbit polyclonal anti-AR (pSer81)	Sigma Aldrich	Cat#07-1375, RRID:AB_11211980
Rabbit monoclonal anti-CDK9 (C12F7)	Cell Signaling Technology	Cat#2316, RRID:AB_2291505
Rabbit monoclonal anti-GAPDH (clone 14C10)	Cell Signaling Technology	Cat#2118, RRID:AB_561053
Mouse monoclonal anti-Pol II (F-12)	Santa Cruz Biotechnology	Cat#sc-55492, RRID:AB_630203
Rabbit polyclonal anti-phospho-AR (Ser81)	Millipore	Cat# 07-1375, RRID:AB_11211980
Mouse monoclonal anti-Mcl-1 (clone 22)	Santa Cruz Biotechnology	Cat# sc-12756, RRID:AB_627915
Rabbit polyclonal to Histone H3 (acetyl K27)	Abcam	Cat#ab4729; RRID: AB_2118291
Rabbit polyclonal anti-Histone H3	Cell Signaling Technology	Cat#9715, RRID:AB_331563
Goat polyclonal IRDye 800CW conjugated anti-rat IgG	LI-COR Biosciences	Cat#926-32219, RRID:AB_1850025
Donkey polyclonal IRDye 800CW conjugated anti-rabbit IgG	LI-COR Biosciences	Cat#926-32213, RRID:AB_621848
Horse HRP-conjugated anti-mouse IgG	Cell Signaling Technology	Cat#7076, RRID: AB_330924
Goat polyclonal HRP-conjugated anti-rabbit IgG	Cell Signaling Technology	Cat#7074, RRID: AB_2099233
Mouse monoclonal anti-beta Actin (clone mAbcam 8226)	Abcam	Cat#ab20272, RRID:AB_445482
Rabbit polyclonal anti-FOXA1	GeneTex	Cat#GTX100308, RRID:AB_1240823
Rabbit monoclonal anti-Acetyl-Histone H3 (Lys27) (clone D5E4)	Cell Signaling Technology	Cat#8173, RRID:AB_10949503
Chemicals, Peptides, and Recombinant Proteins		
KI-ARv-03	This paper	N/A
KB-0742	This paper	N/A
NVP-2	MedChemExpress	Cat#HY-12214A
BAY-1143572 (Atuveciclib)	Selleck Chemicals	Cat#S8727
AZD4573	Selleck Chemicals	Cat#S8719
MC180295	Resynthesized in the Koehler lab.	N/A
R1881	Sigma Aldrich	Cat#R0908
Enzalutamide	SelleckChem	Cat#S1250
Protease and Phosphatase Inhibitor Cocktail	Thermo Scientific	Cat#78440

(Continued on next page)

Continued

REAGENT or RESOURCE	SOURCE	IDENTIFIER
SYPRO-Orange	Molecular Probes	Cat#S6651
TRIzol™ Reagent	Thermo Scientific	Cat#15596018
Halt™ Protease Inhibitor Cocktail	Thermo Scientific	Cat#78430
Dynabeads™ Protein A	Invitrogen	Cat#10008D
Illumina Tagment DNA TDE1 Enzyme and Buffer	Illumina	Cat#20034198
Proteinase K	New England Biolabs	Cat#P8107S
DNA Clean & Concentrator-5	Zymo Research	Cat#D4013
DNase I (RNase-free)	New England Biolabs	Cat#M0303
NEBNext® High-Fidelity 2X PCR Master Mix	New England Biolabs	Cat#M0541
AMPure XP	Beckman Coulter	Cat#A63880
Critical Commercial Assays		
Dual-Glo® Luciferase Assay System	Promega	Cat#E2940
CellTiter-Glo® Luminescent Cell Viability Assay	Promega	Cat#G7572
IncuCyte® Caspase-3/7 Green Apoptosis Assay Reagent	Essen BioScience	Cat#4400
QuantSeq 3′ mRNA-Seq Library Kit for Illumina	Lexogen	Cat#015.
NextSeq 500/550 High Output Kit v2.5 (75 Cycles)	Illumina	Cat#20024906
NextSeq 500/550 High Output Kit v2.5 (150 Cycles)	Illumina	Cat#20024907
Deposited Data		
Structure of CDK9/cyclinT1 in complex with DRB	(Baumli et al., 2010)	PDB: 3MY1
High throughput sequencing dataset	This paper, NCBI GEO: GSE156885	https://www.ncbi.nlm.nih.gov/geo/
Experimental Models: Cell Lines		
Human: VCaP-16 (male)	Laboratory of S.P. Balk, Beth Israel Deaconess Medical Center, Harvard Medical School, Boston, MA 02215, USA	N/A
Human: VCaP (male)	ATCC	Cat#CRL-2876, RRID:CVCL_2235
Human: HEK293T (female)	ATCC	Cat#CRL-3216; RRID: CVCL_0063
Human: DU145 (male)	ATCC	Cat#HTB-81; RRID:CVCL_0105
Human: LNCaP (male)	ATCC	Cat#CRL-1740; RRID:CVCL_1379
Human: PC3 (male)	ATCC	Cat#CRL-1435; RRID:CVCL_0035
Human: 22Rv1 (male)	ATCC	Cat#CRL-2505; RRID:CVCL_1045
Human: MV-4-11 (male)	ATCC	Cat#HTB-189, RRID:CVCL_0064
Experimental Models: Organisms/Strains		
Mouse: CB17-SCID, sex: male	Beijing Vital River Laboratory Animal Technology Co., LTD	N/A
Mouse: BALB/c nude, sex: female	Shanghai Lingchang Biotechnology Co. LTD	N/A
Oligonucleotides: Primers		
GAPDH (qHsaCEP0041396)	Bio-Rad	N/A
KLK3 (qHsaCEP0024737)	Bio-Rad	N/A
KLK3 (Hs02576345_m1)	ThermoFisher	Cat#4331182
AR (Hs00907243_m1)	ThermoFisher	Cat#4331182
Software and Algorithms		
GenePix Pro 6.0	Molecular Devices	http://mdc.custhelp.com/app/answers/detail/a_id/18691/~/genepix%C2%AE-pro-6-microarray-acquisition-%26-analysis-software-download-page
ChemDraw Professional 19.0	PerkinElmer	https://www.perkinelmer.com/product/chemdraw-professional-chemdrawpro

Cell Chemical Biology
Article

CellPress
OPEN ACCESS

Continued

REAGENT or RESOURCE	SOURCE	IDENTIFIER
ImageStudioLite	LI-COR Biosciences	https://www.licor.com/bio/image-studio-lite/download
TIBCO Spotfire®	TIBCO	https://www.tibco.com/products/tibco-spotfire
GraphPad Prism 8	GraphPad	https://www.graphpad.com/scientific-software/prism/
Image Lab 6.0.1	Bio-Rad	https://www.bio-rad.com/en-us/product/image-lab-software?ID=KRE6P5E8Z
SlamDunk	T. Neumann and P. Rescheneder (Neumann et al., 2019)	https://t-neumann.github.io/slamdunk/
High throughput sequencing data analysis protocols	GitHub	https://github.com/linlabcode/cdk9/
AQUAS pipeline	GitHub	https://github.com/kundajelab/chipseq_pipeline
Genialis platform	Genialis, Inc.	https://www.genialis.com/software-applications/
ATAC-seq pipeline	GitHub	https://github.com/kundajelab/atac_dnase_pipelines

RESOURCE AVAILABILITY

Lead Contact
Further information and requests for resources and reagents should be directed to and will be fulfilled by the Lead Contact, Angela N. Koehler (koehler@mit.edu).

Materials Availability
KI-ARv-03 is available through http://koehlerlab.org/contact-us and upon completion of a material transfer agreement by the receiving institution.

Data and Code Availability
Full small molecule screening data sets, along with compound structures for the libraries, are available upon reasonable request. Raw and processed data for all high throughput sequencing experiments performed in this manuscript are available in the NCBI GEO database under the GSE156885 accession number. For analysis of high throughput sequencing data, custom analysis scripts can be found at (https://github.com/linlabcode/cdk9/).

EXPERIMENTAL MODEL AND SUBJECT DETAILS

Animal Studies
The protocol and any amendment(s) or procedures involving the care and use of animals in this study was reviewed and approved by the Institutional Animal Care and Use Committee (IACUC) of WuXi AppTec prior to conduct. During the study, the care and use of animals was conducted in accordance with the regulations of the Association for Assessment and Accreditation of Laboratory Animal Care (AAALAC). The mice were kept in individual ventilation cages at constant temperature and humidity with 5 animals in each cage (Temperature: 20-26°C, Humidity 40-70%). Cages (300 mm × 200 mm x 180 mm) were made of polycarbonate. The bedding material was corn cob, which was changed twice per week. Diet: Animals had free access to irradiation sterilized dry granule food during the entire study period. Water: Animals had free access to sterile drinking water. The identification labels for each cage contained the following information: number of animals, sex, strain, date received, treatment, study number, group number and the starting date of treatment. Animal identification: Animals were marked by ear tags. After inoculation, the animals were checked daily for morbidity and mortality. At the time of routine monitoring, the animals were checked for any effects of tumor growth and treatments on normal behavior such as mobility, food and water consumption, body weight gain/loss (body weight was measured twice weekly, eye/hair matting and any other abnormal effect. Death and observed clinical signs were recorded on the basis of the numbers of animals within each subset. The efficacy studies used 6-8 week-old male CB17-SCID mice (Animal supplier: Beijing Vital River Laboratory Animal Technology Co., LTD., Animal certificate number: 20170011003869) or female BALB/c nude mice (Animal supplier: Shanghai Lingchang biotechnology co. LTD, Animal certificate number: 20180003006523). The cell lines used for transplantation experiments (22Rv1, #CRL-2505; MV-4-11, ATCC, #CRL-9591) were obtained from ATCC.

Cell Lines

Cell lines were obtained from ATCC with exception of VCaP-16 (male, human), which was generated by Joshua Russo in the laboratory of Steven P. Balk. Cell lines were not authenticated in our hands. Cell lines were tested intermittently throughout studies using MycoAlert Mycoplasma Detection Kit (Lonza, Cat#LT07-418), generally a few days after thawing and immediately before significant studies (e.g. RNA-seq experiment). Cells were cultured in a humidified incubator at 37.0°C and 5.0% CO_2. Cell lines used in this study: VCaP (male, human), HEK293T (female, human), DU145 (male, human), LNCaP (male, human), PC3 (male, human), 22Rv1 (male, human), and MV-4-11 (male, human).

METHOD DETAILS

Expression Vector for HA-Tagged Androgen Receptor N-terminal Truncate

The expression vector for HA-tagged AR-ΔLBD truncate was made by cloning the N-terminus of AR (amino acid residues 1-645) from the AR ORF in a pLEX backbone (acquired via the Broad Institute, Genetic Perturbation Platform) into a doxycycline inducible system with an HA tag.

SMM Screening of HA-Tagged AR N-terminal Truncate

Small molecule microarrays were manufactured as previously described (Clemons et al., 2010). Each SMM slide contained approximately 10,000 printed features including 5,000 unique compounds printed in duplicate. In total, 50,000 compounds were screened. Each slide was screened in duplicate for a total of four replicates per compound. HEK293-T cells were plated in 10 cm tissue culture dishes (Corning) in growth media (DMEM supplemented with 1% penicillin-streptomycin solution and 10% fetal bovine serum) at a density of 2×10^6 cells per dish. The following day, cells were transfected with the expression vector for HA-tagged AR-ΔLBD truncate (5 μg DNA per plate) using FuGENE® 6 (Promega) and Opti-MEM media according to the manufacture protocols. Doxycycline (3 μg/mL) was added 4 h after transfection. After 48 h, cells were lysed in 4x volume of RIPA buffer (modified to 250 mM NaCl) supplemented with 2x cOmplete™ protease inhibitor cocktail tablets (Sigma Aldrich) with brief sonication on ice using a microtip sonicator (20 pulses, 30% power, 0.5 s cycle). Lysates were centrifuged for 20 min at 4°C and the concentration of total protein was adjusted to 0.3 mg/mL in MIPP buffer (20 mM NaH_2PO_4, 1 mM Na_3VO_4, 5 mM NaF, 25 mM β-glycerophosphate, 2 mM EGTA, 2 mM EDTA, 1 mM DTT, 0.5% Triton X-100, pH 7.2, cOmplete™ protease inhibitor cocktail tablets) to maintain protein-protein complexes. Each slide was incubated with 3 mL of diluted lysate for 1 h, followed by three consecutive washes with TBS-T. Slides were incubated with an anti-HA.11 mouse monoclonal antibody (BioLegend, #901501) at 1:1000 for 1 h in TBS-T buffer (1X Tris buffered saline, 0.1% Tween-20), followed by three consecutive washes with TBS-T. Slides were then incubated with a Cy3-labeled anti-mouse secondary antibody (Invitrogen) for detection at 1:1000 in TBS-T, followed by three consecutive washes with TBS-T. Slides were briefly rinsed once each in TBS and distilled water and spin-dried. The slides were immediately scanned using a GenePix 4000B fluorescence scanner (Molecular Devices) at PMT 600. The slide images were analyzed using GenePix Pro software (Axon Instruments) to produce raw, numerical data for statistical analysis.

SMM Statistical Analysis

Raw data was analyzed based on the signal-to-noise ratio and reproducibility. For each feature, the signal to noise ratio (SNR) was defined as the median fluorescence intensity of the feature divided by the median fluorescence intensity of the surrounding slide area, defined as a radius 3 times the radius of the spot, excluding pixels within a certain overlap threshold of neighboring features. Then, a robust z-score (Z_i) was calculated for each feature (i) using the following equation:

$$z_i = \frac{SNR_i - Mdn(SNR)}{MAD(SNR) * 1.486}$$

Where SNR_i is the SNR value for a given feature, $Mdn(SNR)$ is the median of the SNR values for all features in the subarray, and the $MAD(SNR)$ is the maximum absolute deviation of the SNR values for all features in the subarray. For each screen, a robust z-score threshold for calling assay positives for further study is chosen independently based on the performance of control feature groups (which serve as "null distribution") in the unique assay.

RT-qPCR for PSA in LNCaP Cells

LNCaP cells were grown in androgen-stripped media (RPMI media supplemented 1% penicillin-streptomycin solution and 10% charcoal stripped fetal bovine serum) for 24 h prior to seeding in 384-well plates at a density of 10,000 cells/well in the same media. After 24 h post-seeding, cells in assay wells were co-treated with 1 nM synthetic androgen (R1881) and compound stocks dissolved in DMSO using a Tecan Freedom EVO 150 S liquid handling system. Cells in control wells were treated either with DMSO alone ("uninduced") or DMSO and 1 nM R1881 ("induced"), again using the same liquid handling system. Following a 24 h compound incubation, media was aspirated from all wells and all wells were rinsed briefly in PBS. Cells were lysed using the BioRad SingleShot Cell Lysis Kit (12 μL total lysis solution per well). Cellular mRNA was reverse transcribed to cDNA using the iScript™ Advanced cDNA Synthesis Kit (Bio-Rad, Hercules, CA, USA) and RT-qPCR was performed using the SsoAdvanced™ Universal Super Probes Mix (Bio-Rad) with PrimePCR™ Probe Assay (Bio-Rad) probes for GAPDH (FAM conjugated, BioRad Unique Assay ID: qHsaCEP0041396) and KLK3 (i.e. PSA, Cy5 conjugated, BioRad Unique Assay ID: qHsaCEP0024737) on the CFX384 Touch™ Real-Time PCR Detection System (Bio-Rad) according to manufacturer specified protocols.

RT-qPCR Data Analysis

Data collected via the CFX Manager™ software (Bio-Rad) was exported to Microsoft® Excel® for analysis. For uninduced and induced control wells, the Ct (cycle threshold) value for each fluorescence channel was taken to be the average Ct value across all respective control wells (n ≥ 10). The ΔCt value for all wells was calculated as the difference between the Ct value in the Cy5 channel (PSA) and the FAM channel (GAPDH) and the ΔΔCt value was calculated as the difference between the ΔCt value of the assay well and the ΔCt value of the induced wells to normalize expression relative to the induced wells. The expression fold change for each well was defined as $2^{(-\Delta\Delta Ct)}$. Average expression fold change for qPCR technical replicates (n = 3) were used to compare compound performance.

Luciferase Reporter Gene Assay

A mouse mammary tumor virus (MMTV)-driven firefly luciferase construct (MMTV-FLuc2P) was used to generate a stable reporter cell line containing doxycycline-inducible AR-V and CMV-driven Renilla luciferase in LNCaP. These cells were grown in androgen-stripped media (RPMI media supplemented with 1% penicillin-streptomycin solution and 10% charcoal stripped fetal bovine serum) for 24 h prior to seeding in 384-well plates at a density of 10,000 cells/well in the same media to reduce the activity of endogenous AR-FL. After seeding for 24 h, cells in assay wells were treated with DMSO, 2 μg/mL doxycycline, or cotreated with 2 μg/mL doxycycline and compound stocks dissolved in DMSO using a Tecan Freedom EVO 150 S liquid handling system. After 24 h post-treatment, luciferase signal was measured using a dual-luciferase reporter assay system (Promega) and a compatible plate reader (Tecan). Raw firefly luciferase signal was normalized for cell count by dividing this value by the raw Renilla luciferase signal on a well-by-well basis. In the absence of compound treatment, the normalized luciferase signal showed ~8-fold induction in the presence of doxycycline compared with vehicle treated control. Averages for replicate wells were calculated and normalized to define doxycycline-treated wells as 1.0 on a plate-by-plate basis to allow comparison of compound performance.

Cell Viability Assays

Prostate cancer cells (LNCaP, VCaP, DU145, PC3) were plated in 384-well plates in appropriate cell culture media (ATCC) at a density empirically determined to produce wells of ~90% confluency five days after seeding for each cellular model. After 24 h post-seeding, cells in assay wells were treated either with DMSO or compound stocks dissolved in DMSO using a Tecan Freedom EVO 150 S liquid handling system. After 72 h of compound exposure, the ATP content in each well was measured as a proxy for cell viability using the CellTiter-Glo® assay system (Promega) and a compatible plate reader (Tecan). Raw luminescence values for each well were averaged across replicate wells and average values were normalized to define DMSO treated wells as 1.0 on a cell line-by-cell line, plate-by-plate basis to compare compound performance.

Lead Evaluation in Cellular CRPC Models

The CRPC cell line VCaP-16 was maintained in DMEM with 10% FBS and 16 μM enzalutamide (SelleckChem, #S1250). 22Rv1 was maintained in RPMI1640 with 10% FBS. For RT-qPCR assays to quantitatively measure PSA, AR-FL, and AR-V7 expression levels, CRPC cells (VCaP-16 or 22Rv1) were plated into 6-well plates in maintenance media at a density of 50%. After 48 h, cells in assay wells were washed twice with PBS then treated either with DMSO or 16 μM enzalutamide plus compound stocks dissolved in DMSO accounting for 5 μM compound concentration. After 18 h of compound exposure, media was aspirated from all samples and each was rinsed briefly in PBS. RNA was isolated and purified using the Qiagen RNeasy Kit (Qiagen) following manufacturer's instructions. Quantitative real-time RT-PCR amplification was performed with TaqMan One-Step RT-PCR reagents (ThermoFisher Scientific) and results were normalized to coamplified β-actin. Primers and probes were purchased from ThermoFisher Scientific and are listed as follows: KLK3 (Hs02576345_m1, FAM-MGB), AR (Hs00907243_m1, FAM-MGB), AR-V7 (Assay ID: AI6ROCI). qRT-PCR was performed on an Applied Biosystems StepONEPLus Real-Time PCR System Thermocycler, according to the manufacturer's specified protocols. The expression fold change for each well was defined as $2^{(-\Delta\Delta Ct)}$ in the manner described above, using actin as the reference gene to define a value of 1.0. Average expression fold change across biological replicates (n = 3) tested in qPCR technical duplicate were used to compare compound performance.

For western blot assays to qualitatively measure AR-FL and AR-V7 protein levels, CRPC cells (VCaP-16 or 22Rv1) were plated in 6-well plates in maintenance cell culture media at a density of 50%. After 48 h, cells in assay wells were washed twice with PBS then treated either with DMSO or 16 μM enzalutamide plus compound stocks dissolved in DMSO accounting for 5 μM compound concentration. After 18 h of compound exposure, media was aspirated from all samples and each was rinsed briefly in PBS. Cells were lysed in RIPA buffer with protease and phosphatase inhibitor cocktail (ThermoScientific, #P78440) on a vortex shaker for 30 min at 4°C. Lysates were spun at 16,000 g for 15 min at 4°C to clarify and pellet aggregated protein. The supernatant containing the soluble protein fraction was transferred to a new tube. Protein lysates were added to loading buffer (2x Laemmli Sample Buffer, Bio-Rad, #1610737) and the samples were boiled at 90°C for 7 min. Samples were electrophoresed at 200 V using a 4-20% denaturing PAGE gel (Bio-Rad). Relative AR-FL, AR-V7 (both detected with AR-N20, Santa Cruz Biotechnology, #sc-816), and β-actin (Abcam, #ab20272) protein levels were determined via immunoblotting.

In Vitro Kinase Activity Assays

KinaseProfiler™ assay to assess broad kinase activity was conducted by Eurofins using 10 μM **KI-ARv-03** and ATP concentrations within 15 μM of the apparent K_m for each kinase. IC_{50}Profiler™ assays were conducted at Eurofins for all kinases showing greater

than 40% reduction of activity in the presence of **KI-ARv-03**. In addition, all available CDKs were tested using IC$_{50}$Profiler™ to generate data included in Figure 2B.

Kinetic studies for ATP competition of **KI-ARv-03** towards CDK9 were conducted using the HotSpot Kinase assay from Reaction Biology Corporation. Here, five different ATP concentrations (1 μM, 10 μM, 50 μM, 100 μM, 200 μM) and four concentrations of **KI-ARv-03** (0.123 μM, 0.370 μM, 1.11 μM, 3.33 μM) were used and the reduction of CDK9 activity monitored over 120 min. These raw data were suggestive of a competitive mode of inhibition and were formally investigated for mode of inhibition using Prism 8.0 (Graph-Pad Software, LLC) to fit these data to a competitive inhibition model described by the following system of equations:

$$\mathbf{K_m^{obs}} = \mathbf{K_m}\left(1 + \frac{\mathbf{[I]}}{\mathbf{K_i}}\right)$$

$$\mathbf{v} = \frac{\mathbf{v_{max}} * \mathbf{[S]}}{\mathbf{K_m^{obs}} + \mathbf{[S]}}$$

Where **[I]** is the concentration of inhibitor, variable across **KI-ARv-03** doses tested; **[S]** is the concentration of substrate, variable across ATP doses tested; **v** is the enzyme velocity; **K$_m^{obs}$** is the apparent Michaelis-Menten constant; **v$_{max}$** is the maximum enzyme velocity without inhibitor; **K$_m$** is the Michaelis-Menten constant; **K$_i$** is the inhibition constant. Global fit parameters for **K$_i$**, **K$_m$**, and **v$_{max}$** are reported in Figure 2C (R^2 = 0.99).

Additional testing of 16 CDK's were performed by Reaction Biology Corporation (RBC) using their HotSpot Kinase Assay to profile **KI-ARv-03** side-by-side with **KB-0742** (Figures 3B and 3C). Compounds were tested in 10-dose in duplicate with a 3-fold serial dilution starting at 10 μM. Control compound, Staurosporine, was tested in 10-dose with 4-fold serial dilution starting at 20 μM. Alternate control compound, **THZ531**, was tested in 10-dose with 3-fold serial dilution starting at 10 μM. Reactions were carried out at K$_m$ ATP according to the RBC K$_m$ binning structure (CDK1/cyclin A (10 μM ATP), CDK12/cyclin K (30 μM ATP), CDK13/cyclin K (5 μM ATP), CDK14/cyclin Y (15 μM ATP), CDK16/cyclin Y (10 μM ATP), CDK17/cyclin Y (20 μM ATP), CDK18/cyclin Y (20 μM ATP), CDK19/cyclin C (20 μM ATP), CDK2/cyclin A (10 μM ATP), CDK3/cyclin E (100 μM ATP), CDK4/cyclin D1 (100 μM ATP), CDK5/P25 (50 μM ATP), CDK6/cyclin D1 (100 μM ATP), CDK7/cyclin H (50 μM ATP), CDK8/cyclin C (10 μM ATP), CDK9/cyclin T1 (10 μM ATP)). Normalized data were plotted and analyzed to produce IC$_{50}$ values in GraphPad PRISM. For all compound:kinase pairs where the top compound concentration tested (10 μM) did not inhibit the kinase by >65% or where the IC$_{50}$ value was outside the range of concentrations tested, the IC$_{50}$ value was set to 10 μM for plotting in the heatmap comprising Figure 3C.

Compound-Anchored Target Engagement
Functionalization of Beads with KI-ARv-03
NHS-functionalized Affi-Gel 10 beads (Bio-Rad Laboratories, Inc., 500 μL, 50% suspension in isopropyl alcohol (IPA)) were pelleted in a 1.5 mL reaction tube by centrifugation (400 x g, 2 min, RT) and washed three times with cold IPA by repeated centrifugation (400 x g, 2 min, RT). Subsequently, the beads were washed three times with anhydrous DMSO (repeated centrifugation, 400 x g, 2 min, RT). After the final wash, the supernatant was removed, and the bead pellet resuspended in 250 μL of anhydrous DMSO to gain a 50% suspension. 200 μL of this suspension each were distributed into fresh 1.5 mL reaction tubes for a) **KI-ARv-03** functionalization as well as b) aminoethanol blocking for control purposes (unspecific protein binding to beads). A solution of **KI-ARv-03** in DMSO (18 μL, 10 mM, theoretical bead loading: 12%) or 5 μL ethanolamine (blocked beads) was added. To each vial Et$_3$N (2.1 μL) was added. The resulting suspensions were shielded from light and allowed and rotate overnight (~16 h) at RT on an overhead rotator. Then 5 μL of ethanolamine were added to each reaction tube in order to block any unreacted NHS-ester. After another 4 h shielded from light on the overhead rotator, the beads were pelleted (400 x g, 2 min, RT). The supernatant was removed, and the beads were washed three times with anhydrous DMSO by repeated centrifugation (400 x g, 2 min, RT). The beads were then washed with PBS three times by repeated centrifugation (400 x g, 2 min, RT) and the pellet was then taken up in as much PBS to account for a final total volume of 200 μL. Distribute beads (40 μL or 60 μL per sample) into new 1.5 mL reaction tubes and add 22Rv1 cell lysate subsequently.
Compound-Anchored Pull-Downs
22Rv1 prostate cancer cells were plated at 200k/mL in 15 cm dishes (30 mL total volume) using phenol red free RPMI media supplemented with 10% FBS (VWR), 1x Pen/Strep (Invitrogen). Cells were harvested at 90% confluency (approx. 2-3 days). Briefly, cells were washed with PBS, and finally collected into 500 μL PBS (2 mL reaction tube) using a cell scraper and then pelleted (300 x g, 3 min, 4°C). The pellet was resuspended in high salt RIPA buffer (50 mM Tris HCl, 400 mM NaCl, 1% (v/v) NP-40, 0.5% (w/v) sodium deoxycholate, 1 mM EDTA, 0.1% (w/v) SDS and 0.01% (w/v) NaN$_3$, pH 7.4) or MIPP buffer (20 mM NaH$_2$PO$_4$, 1 mM Na$_3$VO$_4$, 5 mM NaF, 25 mM β-glycerophosphate, 2 mM EGTA, 2 mM EDTA, 1 mM DTT, 0.5% [v/v] Triton X-100, pH 7.2) supplemented with cOmplete protease inhibitor cocktail (add 4-times volume of pellet). After 30 min of incubation on ice, the cells were sonicated briefly and then centrifuged (15 min, 4300 x g, 4°C). The supernatant was transferred to fresh reaction tubes and the protein concentration quantified using Pierce BCA Protein Assay. For each target engagement assay condition 500 μg lysate were diluted in lysis buffer to make a final volume of 455 μL (40 μL beads used) or 435 μL (60 μL beads used) respectively. For target engagement experiments 5 μL DMSO were added to achieve a final concentration of 1%. For soluble competition experiments 2 μL of 10 mM **KI-ARv-03** in DMSO as well as 3 μL DMSO were added to achieve a final concentration of 40 μM **KI-ARv-03**. The lysates were added to either

Cell Chemical Biology
Article

CellPress
OPEN ACCESS

40 μL or 60 μL **KI-ARv-03**-anchored beads (50% in PBS) to reach a final volume of 500 μL for each target engagement experiment. Samples were incubated shielded from light at 4°C with end-over-end rotation overnight. Samples were then gently centrifuged, and the supernatant removed. The beads were washed three times with cold PBS by repeated centrifugation (200 x g, 3 min) and the supernatant discarded. The beads were resuspended in 100 μL 2x SDS loading buffer and boiled at 95°C for 10 min. After centrifugation (200 x g, 3 min) the supernatant was transferred to fresh tubes and 30 μL of each sample were used for subsequent SDS-PAGE (4-20% denaturing PAGE gel, Bio-Rad) and Western blot analysis.

Cellular Thermal Shift Assay (CETSA)
Protocol adapted from Jafari et al. (Jafari et al., 2014).
Melting Curve
22Rv1 cells (1.0 x 10^6) were washed and harvested with a cell scraper in cold PBS. After transferring to falcon tubes these were spun down (300 x g, 5 min) and the supernatant discarded. The cell pellet was resuspended in 100 μL PBS containing protease inhibitor cocktail and transferred to PCR tubes. Cells were heat shocked in a thermal cycler for 3 min (37°C, 38.6°C, 41.5°C, 46.1°C, 51.5°C, 55.9°C, 59.0°C, 61.0°C, and no heat). The cell suspensions were then subjected to three freeze-thaw cycles with liquid nitrogen to lyse cells. For uniform thawing this step was performed in a thermal cycler at 25°C. Lysates were spun at 21,000 g for 45 min at 4°C to clarify and pellet aggregated protein. The supernatant containing the soluble protein fraction was transferred to a new tube. Protein lysate (7.5 μL) was added to loading buffer (7.5 μL, 2x Laemmli Sample Buffer, Bio-Rad, #1610737) and the proteins were heated to 90°C for 5 min. Samples were electrophoresed at 200 V using a 4-20% denaturing PAGE gel (Bio-Rad). Relative AR (sc-7305, Santa Cruz Biotechnology) and CDK9 (2316S, Cell Signaling Technology) protein levels were determined via immunoblotting.
Dose Response Curve
22Rv1 (1 x 10^6) cells were treated with DMSO or **KI-ARv-03** (0.625 μM, 1.25 μM, 2.50 μM, 5.00 μM, 10 μM, 20 μM, or 40 μM) for 1 h at 37°C. Cells were then washed and harvested with a cell scraper in cold PBS. After transferring to falcon tubes these were spun down for 5 min at 300 x g, and the supernatant discarded. The cell pellet was resuspended in 100 μL PBS containing protease inhibitor cocktail (Millipore Sigma) and transferred to PCR tubes. Cells were heat shocked in a thermal cycler at 49.0°C (or no heat) for 3 min. The cell suspensions were then subjected to three freeze-thaw cycles with liquid nitrogen to lyse cells. For a uniform thawing this step was performed in a thermal cycler at 25°C. Lysates were spun at 21,000 g for 45 min at 4°C to clarify and pellet aggregated protein. The supernatant containing the soluble protein fraction was transferred to a new tube. Protein lysates (7.5 μL) was added to loading buffer (7.5 μL, 2x Laemmli Sample Buffer, Bio-Rad, #1610737) and the proteins were boiled at 90°C for 5 min. Samples were electrophoresed at 200 V using a 4-20% denaturing PAGE gel (Bio-Rad). Relative AR (sc-7305, Santa Cruz Biotechnology) and CDK9 (2316S, Cell Signaling Technology) protein levels were determined via immunoblotting.

Thermal Shift Assays (TSA)
Thermal melting experiments were carried out with an Mx3005p PCR machine (Agilent). CDK9/cyclin T was expressed and purified as described (Baumli et al., 2008) and assayed in a 96-wellplate at a final concentration of 2 μM in a 20 μL volume. Inhibitors were added at a final concentration of 10 μM. SYPRO-Orange (Molecular Probes) was added at a dilution of 1 in 1000. Excitation and emission filters were set to 465 nm and 590 nm, respectively. The temperature was raised with a step of 3°C per minute, and fluorescence readings were taken at each interval as described before (Fedorov et al., 2012).

Immunoblotting
Samples for immunoblotting studies were prepared for electrophoresis by heating (90°C, 5-10 min) in a final concentration of 1x Laemmli loading buffer (supplemented with 5% 2-mercaptoethanol, freshly added). Samples were then electrophorized by SDS-PAGE (4-15% or 4-20% Criterion™ TGX™ Precast gel, BioRad) at a constant voltage within the range of 160 – 200 V. Proteins were transferred to a nitrocellulose membrane (BioRad) using the Trans-Blot® Turbo™ transfer system (BioRad). Membranes were blocked with 5% BSA in TBS-T for a minimum of 1 h (RT) before incubating with the following primary antibodies (unless otherwise specified): Pol II Antibody (F-12) #sc-55492 (Santa Cruz Biotechnology), RNA polymerase II CTD repeat YSPTSPS (pSer2) antibody #ab5095 (Abcam), AR Antibody (441) #sc-7305 (Santa Cruz Biotechnology), anti-phospho-Androgen Receptor (pSer81) #07-1375 (Sigma Aldrich), Histone H3 antibody #9715 (Cell Signaling Technology), Pol II pS2 #04-1571 (Sigma Aldrich), Pol II pS5 #04-1572 (Sigma Aldrich), Pol II pS7 #04-1570-I (Sigma Aldrich), CDK9 #2316 (Cell Signaling Technology), GAPDH #2118 (Cell Signaling Technology), MYC #sc-40 (Santa Cruz Biotechnology), MCL-1 #sc-12756 (Santa Cruz Biotechnology). Secondary antibodies were either anti-mouse or anti-rabbit HRP linked antibodies (BioRad) for imaging on a ChemiDoc™ imaging system (BioRad) or anti-mouse, anti-rabbit IR800 antibodies or anti-rat 800CW and 680LT (LI-COR Biotechnology) for all for imaging on an Odyssey CLx (LI-COR Biotechnology). For crossblotting, Restore™ PLUS (Thermo Fischer Scientific) or NewBlot™ (LI-COR Biotechnology) Western Blot Stripping Buffer was used according to manufacturer protocols prior to re-probing with the appropriate primary antibody.

Growth Rate Inhibition Studies
22Rv1 cells were plated in 96-well plates, adding 100 μL of a 75,000 cells/mL cell suspension in RPMI media (7,500 cells per well). After 24 h, cell culture media for 22Rv1 cells was removed and replaced with media containing 5 μM of IncuCyte® Caspase-3/7 Green Apoptosis Assay Reagent (Essen Bioscience) according to manufacturer protocol and either DMSO or CDK9 inhibitor dissolved in DMSO at the appropriate final concentration. MV-4-11 cells were plated in 96-well plates after treating plates with fibro-

nectin (1 μg/cm^2 in PBS, 40 μL/well, 1 h, RT), removing excess PBS, and adding 80 μL of a 62,500 cells/mL cell suspension in IMDM media (5,000 cells per well). Plate was spun for 1 min at 200 x g after plating of cells. After 24 h, 40 μL of a mixture containing In-cuCyte® Caspase-3/7 Green Apoptosis Assay Reagent (Essen Bioscience, 5 μM final concentration) and CDK9 inhibitor in DMSO at the appropriate concentrations or DMSO alone in IMDM were added. Plates were then imaged over a period of 72 h (22Rv1) or 48 h (MV-4-11), collecting four images per well every 3 h with a 10x objective using the IncuCyte® S3 in a standard tissue culture incubator. The resultant images were analyzed for confluency and apoptotic signal using the associated IncuCyte® S3 soft-ware, adjusting the mask and filter settings for image analysis using a small training set of images (~12) from DMSO control wells and high doses of compound at early and late time points. To determine growth rate inhibition (GR) metrics, confluency data for com-pound-treated wells at the assay endpoint and DMSO wells at t = 0 and the assay endpoint were used as inputs to GRcalculator, an online tool for calculating and mining dose-response data hosted by Harvard Medical School (HMS) LINCS (Library of Integrated Network-based Cellular Signatures) Center. Finally, the number of caspase-3/7 positive cells for each condition over time were used to calculate AUC values for cleaved caspase accumulation using GraphPad PRISM 8.0.

Thiol(SH)-Linked Alkylation for the Metabolic Sequencing of RNA (SLAM seq)
SLAM seq experiments were performed as described before (Herzog et al., 2017). In brief, 22Rv1 carcinoma cells were seeded at 60% confluency 18 h before being pretreated with 800 μM s4U (Sigma, St. Louis, MO) to start the pulse. The cells were incubated in the media with s4U and the 0 h samples were collected after 30 min by washing the cells with PBS and lysing directly with TRIzol (Invitrogen, Carlsbad, CA). The media was replaced with media containing 800 μM s4U along with either DMSO, **KB-0742** (1.2 μM) or **KI-ARv-03** (4 μM) and they were collected similarly after 2, 4 or 8 h post incubation. The RNA from the cells were harvested by total RNA extraction in the presence of 0.1 mM DTT to maintain the samples in reducing conditions and the extracted RNA was resus-pended with 1 mM DTT. The ERCC RNA Spike-in control mix was added to each sample and thiol modifications were performed by treating 1.5 μg of total RNA with freshly prepared Iodoacetamide (IAA) at a final concentration of 10 mM. The reactions were quenched, and the thiol modified RNA was ethanol precipitated. The libraries were prepared using the QuantSeq 3′ mRNA-Seq Li-brary Prep Kit (Lexogen, Vienna, Austria) and were sequenced with NextSeq 500/550 High Output Kit v2.5 (75 Cycles) (Illumina, San Diego, CA). Reads were aligned to a bed of 3′ UTR regions (hg19_RefSeq_Curated_3UTR.bed) drawn from the UCSC hg19 genome reference using the SLAM Seq processing pipeline SlamDunk (https://t-neumann.github.io/slamdunk/) (Neumann et al., 2019). Custom analysis scripts can be found at (https://github.com/linlabcode/cdk9/).

Analysis was performed on a set of 4,852 highly transcribed active genes. These were defined as having at least one sample with total reads (counts per million) in the top 25 percentile for which nascent (converted reads) transcripts could be detected. To quantify levels of nascent transcription, we utilized the fraction converted reads as output by SlamDunk to represent the nascent mRNA frac-tion. For instance, a value of 0.1 would indicate that 10% of reads for a gene are metabolically labeled and therefore nascently transcribed.

Samples were hierarchically clustered by nascent mRNA fraction levels at top active transcribed genes (Figure S5C). Profiles of mean log$_2$ fold change at each timepoint relative to matched DMSO control were hierarchically clustered by both row (genes) and columns (samples) (Figure 5A). In both cases a distance metric of 1 – Pearson correlation was used.

To identify differentially transcribed genes, nascent mRNA fraction was compared between treatment and DMSO control samples. A p-value threshold of <0.01 was used to identify differential genes. Changes in nascent mRNA fraction were compared between **KI-ARv-03** and **KB-0742** and assessed using a Pearson correlation (Figure S5D). Genes in the top 50 by nascent mRNA fraction in DMSO control samples were annotated as top transcribed genes (Figure 5B). For changes in nascent mRNA fraction at individual genes, bar plots are used with the error bars representing standard error of the mean (Figure 5C).

Chromatin Immunoprecipitation (ChIP)
Chromatin immunoprecipitations were performed using the ChIPmentation protocol as described previously (Schmidl et al., 2015) with minor modifications. Briefly, 15 x 10^6 (for FOXA1 ChIP) or 8 x 10^5 (for H3K27ac ChIP) 22Rv1 carcinoma cells were treated for 24 h with DMSO and were crosslinked by incubating in formaldehyde to a final concentration of 0.8% for 5 min at room temperature The fixation was terminated by adding Glycine to a final concentration of 125 mM and incubation on a rocker at RT for 5 min. The cells were washed in ice cold PBS buffer thrice and the cells were harvested using a cell lifter. The crosslinked cells were then lysed in L1 buffer (50 mM HEPES, 140 mM NaCl, 1 mM EDTA, 10% Glycerol, 0.5% IGEPAL and 0.25% Triton X-100) with protease inhibitor (PI) at 4°C in a rotor. The cells were pelleted and resuspended in L2 buffer (200 mM NaCl, 1 mM EDTA, 0.5 mM EGTA in 10 mM Tris) with PI and incubated at RT in a rotor. The nuclei were pelleted by centrifugation at 4°C and were washed twice with the sonication buffer (SE) (10 mM Tris, 1 mM EDTA, 0.1% SDS). The pellet was resuspended in SE with PI and was sheared using a covaris LE220 sonicator (Covaris, Woburn, MA) for 12-14 minutes (FOXA1 assay) or 6.5 min (H3K27ac assay). Sonicated lysates were supplemented with salts and detergents to a final concentration of 1% Triton X-100, 150 mM NaCl and 0.1% Na-deoxycholate. The chromatin was then cleared by centrifugation and incubated with Dynabeads™ Protein A (Thermo Fisher Scientific, Waltham, MA) for 1 h to preclear the lysate. After collecting the input, the supernatant was incubated with end-over-end rotation overnight at 4°C with Dynabeads™ Protein A magnetic beads prebound with antibody (2 μL anti-H3K27ac (Cell Signaling Technology, #8173) for H3K27ac ChIP and 6 μL anti-FOXA1 (GeneTex, #GTX100308) for FOXA1 ChIP). The antibody was bound to the beads by incubating the beads with the anti-body in 200 μL of bead binding buffer (10 mM Tris, 1 mM EDTA, 0.2% IGEPAL) in a rotor at 4°C for 2 h. Beads were washed once with low salt wash buffer (250 mM NaCl, 10 mM Tris-HCl, 1 mM EDTA, 0.1% SDS, 0.1% Na-deoxycholate, 0.1% Triton X-100), once with

Cell Chemical Biology
Article

high salt wash buffer containing 500 mM NaCl, once with LiCl wash buffer (20 mM Tris pH 8.0, 1 mM EDTA, 250 mM LiCl, 0.5% NP-40, 0.5% Na-deoxycholate), once with wash buffer containing 10 mM Tris, 1 mM EDTA, 0.1% Triton X-100 and twice with ice cold 10 mM Tris-HCl. The beads and the input were then incubated at 37°C with the Tagment DNA enzyme (Illumina) following tagmentation. The beads were washed twice with the low salt wash buffer and DNA was eluted with 10 mM Tris, 1 mM EDTA, 250 mM NaCl and 0.3% SDS. Cross-links were reversed by initial incubation at 55°C and continued with protein digestion with the addition of Proteinase K (New England Biolabs, Boston, MA) for 10 h at 64°C. DNA was purified using a DNA Clean & Concentrator-5 Kit (Zymo Research, Irvine, CA).

ChIP data was processed using Genialis platform and the data analysis pipeline resembles the AQUAS pipeline (https://github.com/kundajelab/chipseq_pipeline). ChIP-seq, ChIPmentation, and ChIP-exo undergo the same procedure: Reads are aligned to hg19 genome using BWA-ALN. Then reads are filtered and only mapped reads, primary alignments, and reads with mapping quality greater than 30 are kept. In case of paired-end reads only properly mapped pairs are kept. Subsequently, duplicate reads are removed using picard-tools MarkDuplicates and samtools. Fragment length is estimated using spp. Finally, peaks are called using MACS2 with p-value set to 1×10^{-05} and without building a model, using the previously estimated fragment length.

Omni Assay for Transposase-Accessible Chromatin (Omni-ATAC)
Omni ATAC-seq was performed as previously described (Corces et al., 2017). 50,000 live cells in culture medium were treated with DNase at a final concentration of 200 U/mL at 37°C for 30 minutes. The cells were washed thrice with PBS to remove DNase followed by lysis with RSB (10 mM Tris-HCl, 10 mM NaCl, 3 mM MgCl$_2$) containing 0.1% NP40, 0.1% Tween-20, and 0.01% Digitonin and mixed by pipetting up and down thrice. The cells were lysed on ice for 3 min and the reaction was stopped by adding 1 mL of ice cold RSB containing 0.1% Tween-20 and mixed by inverting the tubes thrice. The nuclei were pelleted by centrifugation at 4°C and the pellet was resuspended in 50 μL of transposition mix (25 μL 2x TD buffer, 2.5 μL transposase, 16.5 μL PBS, 0.5 μL 1% digitonin, 0.5 μL 10% Tween-20, 5 μL H$_2$O) and was incubated at 37°C for 30 min with mixing. The reaction was then cleaned up with a Zymo DNA Clean and Concentrator-5 Kit.

ATAC data was processed using Genialis platform and the data analysis pipeline resembles the ATAC-seq pipeline (https://github.com/kundajelab/atac_dnase_pipelines). Reads are aligned to hg19 genome using Bowtie2. Then reads are filtered and only mapped reads, primary alignments, properly mapped pairs, and reads with mapping quality greater than 30 are kept. Subsequently, duplicate reads are removed using picard-tools MarkDuplicates and samtools. Then Tn5 transposon shifting is performed. Finally, peaks are called using MACS2 with p-value set to 0.01 and without building a model, using the fragment length of 150 and shiftsize of 75.

Library Preparations
Library preparations for the ChIP and ATAC samples were performed as previously described (Buenrostro et al., 2015) with minor changes. In brief, to generate multiplexed libraries, a preamplification cycle was performed with the transposed DNA. The DNA was amplified for five PCR cycles with Illumina indexed primers (Nextera index kit, Illumina), 25 μL of NEBNext High-Fidelity 2x PCR Master Mix (New England Biolabs). 5 μL of this amplified DNA was amplified further using qPCR to determine the appropriate number of PCR cycles needed to achieve maximum amplification with minimum duplicates. The number of cycles needed was calculated by determining the cycle number that corresponds to 25% of the maximum fluorescence intensity. The final amplification was performed with the leftover (45 μL) from the preamplification reaction using the number of cycles calculated in the qPCR. The amplified libraries were cleaned, and size selected using AMPure XP (Beckman Coulter, Indianapolis, IN) and were validated for quality and size distribution using a TapeStation 2200 (Agilent, Santa Clara, CA). The libraries were sequenced using NextSeq 500/550 High Output Kit v2 (75 cycles) (Illumina) for ChIP-seq and NextSeq 500/550 High Output Kit v2 (150 cycles) (Illumina) for ATAC-seq in a NextSeq 550 (Illumina).

22Rv1 Human Prostate Cancer Xenograft Model in Male CB17-SCID Mice
Xenograft studies were performed at WuXi AppTec Co., Ltd., (Shanghai, China).
Cell Culture
22Rv1 tumor cells (ATCC, CRL-2505) were maintained *in vitro* as a monolayer culture in RPMI-1640 medium supplemented with 10% fetal bovine serum, 1% Antibiotic-Antimycotic at 37°C in an atmosphere of 5% CO$_2$. The tumor cells were routinely subcultured twice weekly by 0.25% trypsin-EDTA treatment. The cells growing in an exponential growth phase were harvested and counted for tumor inoculation.
Tumor Implantation and Treatment
Each mouse (*Mus musculus,* male, strain: CB17-SCID, age: 6-8 weeks, body weight: 18-22 g) was inoculated subcutaneously at the right flank with 22Rv1 tumor cells (2×10^6) in 0.2 mL of PBS supplemented with BD Matrigel (1:1) for tumor development. Animals were randomized and treatment started when the average tumor volume reached approximately 170 mm^3. Mice were treated at 10 μL/g body weight either with vehicle (10% EtOH, 20% PEG400, and 70% (20% HPβCD), p.o., QD, 21 days), 15 mg/kg Docetaxel (i.p., QW, 3 weeks), 3 mg/kg **KB-0742** (p.o., QD, 21 days), 10 mg/kg **KB-0742** (p.o., QD, 21 days), 30 mg/kg **KB-0742** (p.o., QD, 21 days), or 3 mg/kg **KB-0742** (p.o., QD, 21 days (3-day on/4-day off)).

MV-4-11 Human AML Xenograft in Female BALB/c Nude Mice

Cell Culture

MV-4-11 tumor cells (ATCC, CRL-9591) were maintained *in vitro* as a suspension culture in RPMI1640 medium supplemented with 10% heat inactivated fetal bovine serum, 100 U/mL penicillin and 100 μg/mL streptomycin at 37°C in an atmosphere of 5% CO_2. The cells growing in an exponential growth phase were harvested and counted for tumor inoculation.

Tumor Implantation and Treatment

Each mouse (*Mus musculus*, female, strain: BALB/c nude, age: 6-8 weeks, body weight: 19-21 g) was inoculated subcutaneously at the right flank with MV4-11 tumor cells (10×10^6) in 0.2 mL of PBS supplemented with BD Matrigel (1:1) for tumor development. The animals were randomized and treatment started when the average tumor volume reached 154 mm^3. Mice were treated at 10 μL/g body weight either with vehicle (10% EtOH, 20% PEG400, and 70% (20% HPβCD), p.o., QD, 21 days), 25 mg/kg **KB-0742** (p.o., QD, 21 days), 15 mg/kg **KB-0742** (p.o., QD, 21 days (3-day on/4-day off)), 30 mg/kg **KB-0742** (p.o., QD, 21 days (3-day on/4-day off)), or 60 mg/kg **KB-0742** (p.o., QD, 21 days (3-day on/4-day off)).

Tumor Measurement and Endpoints

Tumor size was measured twice weekly in two dimensions using a caliper, and the volume was expressed in mm^3 using the formula:

$$V = 0.5 \text{ a x b}^2$$

Where **a** and **b** are the long and short diameters of the tumor, respectively. Tumor growth inhibition (TGI) was calculated for each group using the formula:
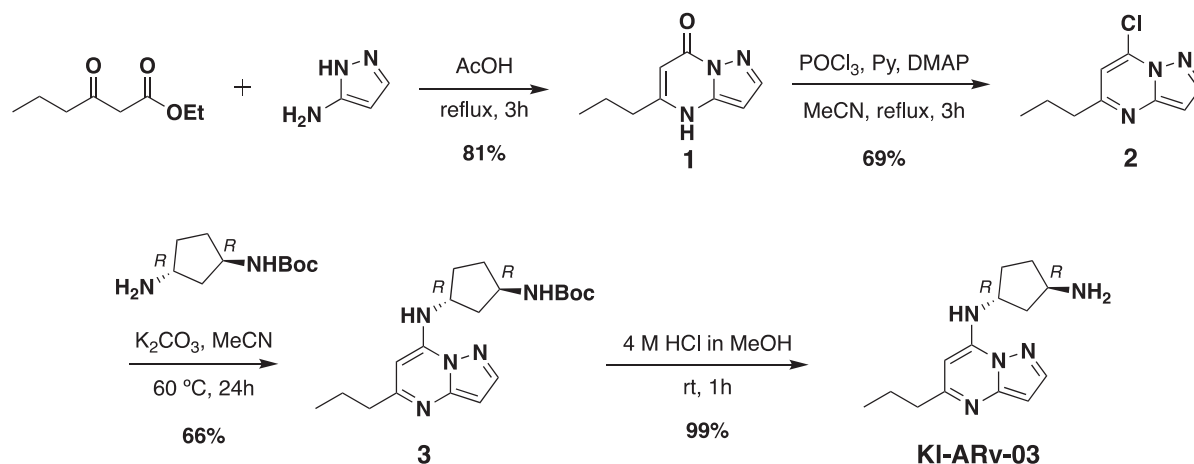
$$\text{TGI (\%)} = [1-(T_i-T_0)/(V_i-V_0)] \times 100$$

Where T_i is the average tumor volume of a treatment group on a given day, T_0 is the average tumor volume of the treatment group on the first day of treatment, V_i was the average tumor volume of the vehicle control group on the same day with T_i, and V_0 was the average tumor volume of the vehicle group on the first day of treatment. Tumor volume was measured at study termination. The **T/C** value (in percent) was calculated where **T** and **C** are the mean tumor volume of the treated and control groups, respectively. Animal body weight was monitored regularly as an indirect measure of toxicity. On day nine of treatment, one mouse of the Docetaxel (15 mg/kg) and one mouse of the **KB-0742** (30 mg/kg) treatment regimen were sacrificed due to the body weight loss >20% in the 22Rv1 Human Prostate Cancer Xenograft Model.

Statistical Analysis

Summary statistics, including mean and the standard error of the mean (SEM), are provided for the tumor volume of each group at each time point (Tables S3 and S5). Statistical analysis of difference in the tumor volume among the groups was conducted on the data obtained at the best therapeutic time point after the final dose (day 21 of treatment 22Rv1, day 16 of treatment MV-4-11, Tables S4 and S6). A one-way ANOVA was performed to compare the tumor volume and the tumor weights among groups, comparisons between groups were carried out with Games-Howell (22Rv1) or Dunnett t (2-sided) (MV-4-11). All data were analyzed using SPSS 17.0. $p < 0.05$ was considered to be statistically significant.
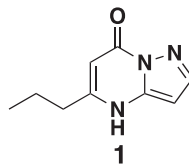
Chemical Synthesis

KI-ARv-03 Synthesis

Scheme 1: Synthetic Procedure to Yield Probe Molecule KI-ARv-03

Cell Chemical Biology
Article

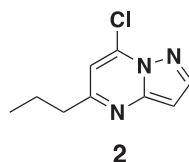**CellPress**
OPEN ACCESS

5-propylpyrazolo[1,5-a]pyrimidin-7(4H)-one (1).

1

A solution of 3-Aminopyrazole (14.5 g, 175 mmol) and ethyl 3-oxoethanoate (29.4 mL, 184 mmol) in glacial acetic acid (100 mL) was refluxed for 3 h. After cooling to room temperature, the solvent was removed under reduced pressure and residuals were suspended in EtOAc. The resulting mixture was filtered and the remaining solid was washed with EtOAc (3 x 100 mL) to yield **1** as an off-white solid (25.1 g, 142 mmol, 81%).

¹H NMR (400 MHz, DMSO-d_6): δ 12.22 (s, 1H), 7.82 (d, J = 2.0 Hz, 1H), 6.10 (d, J = 2.0 Hz, 1H), 5.58 (s, 1H), 2.55 – 2.49 (m, 2H), 1.66 (h, J = 7.4 Hz, 2H), 0.91 (t, J = 7.4 Hz, 3H). **¹³C NMR** (101 MHz, DMSO-d_6): δ 156.53, 153.79, 142.75, 141.71, 94.28, 88.46, 34.21, 21.27, 13.31. **LC-MS (ES⁺)**: m/z 178.1.
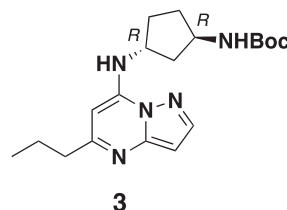
7-chloro-5-propylpyrazolo[1,5-a]pyrimidine (2).

2

To a suspension of 5-propylpyrazolo[1,5-*a*]pyrimidin-7-ol (**1**, 801 mg, 4.52 mmol) in dry MeCN were added phosphorous oxychloride (1.68 mL, 18.1 mmol, dropwise), pyridine (438 μL, 5.42 mmol), and dimethylaminopyridine (28 mg, 0.23 mmol). The resulting suspension was refluxed for 3 h. After cooling to room temperature, the solvent was removed in vacuo and the remaining residue was treated with ice water and immediately extracted with EtOAc (3 x 100 mL). The combined organic layers were dried with Na₂SO₄ and the crude was purified by silica gel flash column chromatography (0-30% EtOAc/hexane) to yield **2** as yellow/green liquid (611 mg, 3.12 mmol, 69%). The product was used immediately for subsequent reactions.

¹H NMR (500 MHz, DMSO-d_6): δ 8.27 (d, J = 2.3 Hz, 1H), 7.36 (s, 1H), 6.75 (d, J = 2.3 Hz, 1H), 2.77 (t, J = 7.5 Hz, 2H), 1.74 (h, J = 7.4 Hz, 2H), 0.92 (t, J = 7.4 Hz, 3H). **¹³C NMR** (DMSO-d_6): δ 162.27, 149.05, 145.14, 137.33, 108.79, 97.04, 39.08, 21.23, 13.58. **LC-MS (ES⁺)**: m/z 197.1 and 198.0 [M+H]⁺
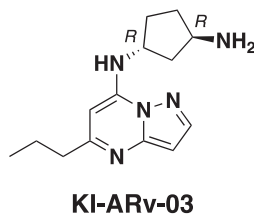
tert-butyl ((1R,3R)-3-((5-propylpyrazolo[1,5-a]pyrimidin-7-yl)amino)cyclopentyl) carbamate (3).

3

To a solution of 7-chloro-5-propylpyrazolo[1,5-*a*]pyrimidine (**2**, 400 mg, 2.04 mmol) in MeCN were added tert-butyl ((1R,3R)-3-aminocyclopentyl)carbamate (429 mg, 2.14 mmol) and K₂CO₃ (563 mg, 4.08 mmol). The resulting suspension was stirred at 60°C for 16 h. After cooling to room temperature, the reaction mixture was diluted with water and extracted with DCM (3 x 100 mL). The combined organic layers were dried over Na₂SO₄ and the crude was purified by flash column chromatography (0-70% EtOAc/hexane) to yield **3** as a light-brown resin (481 mg, 1.34 mmol, 66%).

¹H NMR (500 MHz, DMSO-d_6): δ 7.99 (d, J = 2.2 Hz, 1H), 7.61 (d, J = 7.9 Hz, 1H), 6.97 (d, J = 7.5 Hz, 1H), 6.28 (d, J = 2.3 Hz, 1H), 6.05 (s, 1H), 4.17 (h, J = 7.3 Hz, 1H), 3.97 (h, J = 6.6 Hz, 1H), 2.61 (dd, J = 8.4, 6.7 Hz, 2H), 2.13 (dtd, J = 12.6, 7.9, 4.6 Hz, 1H), 2.08 – 1.94 (m, 1H), 1.96 – 1.84 (m, 2H), 1.76 – 1.64 (m, 3H), 1.52 – 1.41 (m, 1H), 1.38 (s, 9H), 0.92 (t, J = 7.3 Hz, 3H). **LC-MS (ES⁺)**: m/z 360.5 [M+H]⁺
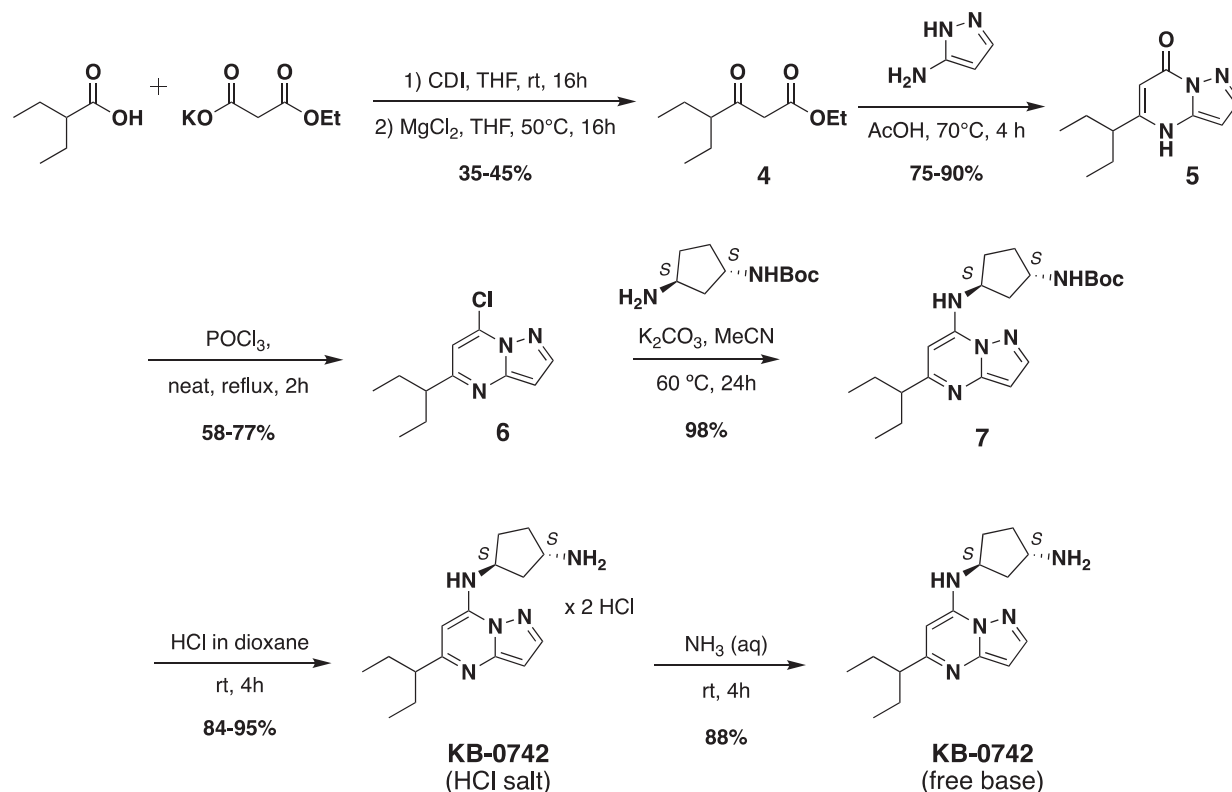
*(1*R,3R)-N^1-(5-propylpyrazolo[1,5-a]pyrimidin-7-yl)cyclopentane-1,3-diamine (KI-ARv-03).*

KI-ARv-03

tert-butyl ((1*R,3R*)-3-((5-propylpyrazolo[1,5-*a*]pyrimidin-7-yl)amino)cyclopentyl) carbamate (**3**, 481 mg, 1.34 mmol) was treated with a solution of 4 M HCl in MeOH for 1.5 h at room temperature. The solution was basified with saturated Na$_2$HCO$_3$ solution and extracted with DCM. The combined organic layers were dried over Na$_2$SO$_4$ and the solvent was removed in vacuo to yield **KI-ARv-03** as brown syrup (343 mg, 1.33 mmol, 99%).
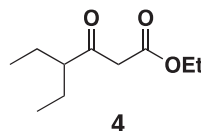
^{1}H NMR (DMSO-*d$_6$*): δ 7.99 (d, *J* = 2.3 Hz, 1H), 7.44 (s, 1H), 6.28 (d, *J* = 2.2 Hz, 1H), 6.03 (s, 1H), 4.21 (t, *J* = 7.3 Hz, 1H), 3.43 (p, *J* = 5.8 Hz, 1H), 2.61 (dd, *J* = 8.4, 6.7 Hz, 2H), 2.20 (dtd, *J* = 12.9, 7.9, 4.9 Hz, 1H), 2.00 – 1.83 (m, 3H), 1.83 – 1.58 (m, 5H), 1.30 (dtd, *J* = 13.2, 8.0, 5.4 Hz, 1H), 0.92 (t, *J* = 7.4 Hz, 3H). **^{13}C NMR** δ (101 MHz, DMSO-*d$_6$*) δ 162.26, 148.77, 146.00, 142.99, 93.59, 84.91, 51.59, 51.07, 41.97, 39.84 34.19, 30.66, 21.93, 13.76. **LC-MS (ES$^+$)**: m/z 260.4 [M+H]$^+$

KB-0742 Synthesis

Scheme 2: Synthetic Procedure to Yield Advanced Molecule KB-0742
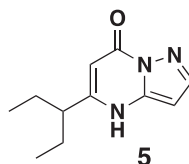
Ethyl 4-ethyl-3-oxohexanoate (4).

4

2-Ethylbutanoic acid (7.5 g, 64.6 mmol) was dissolved in THF (150 mL) and cooled to 0°C. Within 20 min CDI (16.23 g, 100.1 mmol) was added portion-wise. The reaction warmed to room temperature (rt) and the mixture (referred to as "solution A") was stirred at rt

Cell Chemical Biology
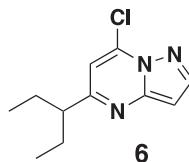## Article

CellPress
OPEN ACCESS

overnight. In a second flask $MgCl_2$ (6.14 g, 64.6 mmol) and potassium 3-ethoxy-3-oxo-propanoate (17 g, 100.1 mmol) were mixed with THF (150 mL) and stirred under argon overnight at 50°C. The resultant white suspension was cooled to rt and solution A was added dropwise over 10 min and the reaction mixture was stirred for 16 h at rt. After several minutes a sticky, amorphous solid appeared whereupon after several hours the reaction mixture becomes homogenous in appearance. The reaction mixture was concentrated to about a third, taken up in half sat. potassium bisulphate solution and extracted twice with ethyl acetate. The combined organic layers were washed with a sat. sodium bicarbonate solution, combined, dried over anhydrous sodium sulfate, filtered and the solvent was evaporated. Purification by column chromatography gave ethyl 4-ethyl-3-oxo-hexanoate (4.3 g, 23.1 mmol, 36%) as a clear liquid. The RM was monitored by TLC (10% EtOAc/hexane, Product R_f = 0.6, SM R_f = 0.1). **¹H NMR** (400 MHz, DMSO-d_6) δ 4.08 (q, J = 7.1 Hz, 2H), 3.59 (s, 2H), 2.49 – 2.38 (m, 1H), 1.68 – 1.34 (m, 4H), 1.18 (t, J = 7.0 Hz, 3H), 0.84 – 0.75 (m, 6H). **LC-MS** (m/z 186.13, found 187.0 [M+H⁺]).

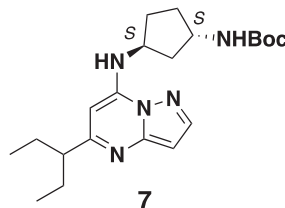*5-(pentan-3-yl)pyrazolo[1,5-a]pyrimidin-7(4H)-one (5).*

To a suspension of ethyl 4-ethyl-3-oxo-hexanoate (**4**, 4.4 g, 23.6 mmol) in acetic acid (11 mL) at 70°C was added 1*H*-pyrazol-5-amine (4.71 g, 56.7 mmol) in two portions (the second portion was added after 2 h of stirring the first portion) over a 4 h period. The reaction was cooled to rt and the solvent was evaporated under reduced pressure. The residue was treated with ethyl acetate and filtered to give 5-(pentan-3-yl)pyrazolo[1,5-a]pyrimidin-7(4*H*)-one (3.7 g, 17.7 mmol, 75%) as an off-white solid. The reaction mixture was monitored by TLC (5% MeOH/DCM, Product R_f = 0.3, SM R_f = 0.8). **¹H NMR** (400 MHz, DMSO-d_6) δ 12.05 (s, 1H), 7.84 (s, 1H), 6.12 (s, 1H), 5.59 (s, 1H), 2.42–2.31 (m, 1H), 1.71–1.52 (m, 4H), 0.81 (t, J = 7.4 Hz, 6H). **¹³C NMR** (100 MHz, DMSO-d_6) δ 156.38, 156.31, 142.49, 141.57, 93.60, 88.49, 46.71, 26.30, 11.52. **LC-MS** (m/z 205.12, found 206.4 [M+H⁺]).

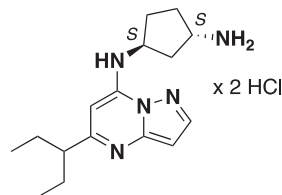*7-chloro-5-(pentan-3-yl)pyrazolo[1,5-a]pyrimidine (6).*

A stirred solution of 5-(pentan-3-yl)pyrazolo[1,5-a]pyrimidin-7(4*H*)-one (**5**, 3.7 g, 18.0 mmol) in $POCl_3$ (33.7 mL, 360.5 mmol) was heated to reflux for 4 h. The reaction mixture was cooled to rt, excess reagent was evaporated in a rotary evaporator, and the residue was treated with ice-water. The chlorinated product was immediately extracted with DCM. The organic layer was separated, dried over anhydrous Na_2SO_4, filtered and purified by column chromatography to yield 7-chloro-5-(pentan-3-yl)pyrazolo[1,5-a]pyrimidine (3.1 g, 13.9 mmol, 77%) as a light yellow liquid. The reaction mixture was monitored by TLC (20% EtOAc/hexane, Product R_f = 0.6, SM R_f = 0.1). **¹H NMR** (400 MHz, CDCl₃) δ 8.16 (s, 1H), 6.81 (s, 1H), 6.69 (s, 1H), 2.69–2.52 (m, 1H), 1.84–1.64 (m, 4H), 0.87–0.81 (m, 6H). **¹³C NMR** (100 MHz, CDCl₃) δ 165.61, 149.62, 145.25, 138.35, 107.49, 97.50, 51.59, 27.64, 11.99. **LC-MS** (m/z 223.09, found 224.3 [M+H⁺]).

tert-*butyl ((1S,3S)-3-((5-(pentan-3-yl)pyrazolo[1,5-a]pyrimidin-7-yl)amino)cyclopentyl) carbamate (7).*
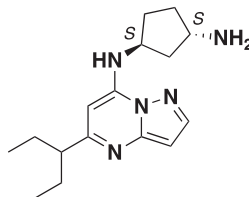

To a stirred solution of 7-chloro-5-(pentan-3-yl)pyrazolo[1,5-*a*]pyrimidine (**6**, 500 mg, 2.24 mmol) in MeCN (10 mL) tert-Butyl ((1S,3S)-3-aminocyclopentyl)carbamate (447.7 mg, 2.24 mmol) and K_2CO_3 (925 mg, 6.71 mmol) were added and the resulting reaction mixture was heated to reflux for 16 h. The reaction mixture was filtered, concentrated under reduced pressure and purified by column chromatography (30% EtOAc/hexane) to give tert-butyl ((1S,3S)-3-((5-(pentan-3-yl)pyrazolo[1,5-a]pyrimidin-7-yl)amino)cyclopentyl)carbamate (850 mg, 2.19 mmol, 98% yield) as an off-white solid. The reaction mixture was monitored by TLC (40% EtOAc/hexane, Product R_f = 0.5, SM R_f = 0.7). **¹H NMR** (400 MHz, CDCl₃) δ 7.92 (d, J = 2.3 Hz, 1H), 6.41 (d, J = 2.2 Hz, 1H), 6.17 (d, J = 6.8 Hz, 1H), 5.73 (s, 1H), 4.54 (s, 1H), 4.19–4.06 (m, 2H), 2.53–2.40 (m, 1H), 2.41–2.18 (m, 2H), 2.15–1.99 (m, 2H), 1.78–

1.68 (m, 4H), 1.63–1.49 (m, 1H), 1.44 (s, 9H), 0.84 (t, J = 7.4 Hz, 6H). ^{13}**C NMR** (400 MHz, DMSO-d_6) δ 165.12, 154.91, 148.83, 145.94, 142.93, 93.66, 84.83, 77.43, 51.18, 50.98, 49.84, 38.40, 31.18, 30.06, 28.19, 27.29, 12.01 **LC-MS** (m/z 387.26, found 388.3 [M+H$^+$]). *(1S,3S)-N^1-(5-(pentan-3-yl)pyrazolo[1,5-a]pyrimidin-7-yl)cyclopentane-1,3-diamine hydrochloride (KB-0742 x 2 HCl).*

KB-0742
(HCl salt)

To *tert*-butyl ((1S,3S)-3-((5-(pentan-3-yl)pyrazolo[1,5-a]pyrimidin-7-yl)amino)cyclopentyl) carbamate (**7**, 1.0 g, 2.58 mmol) in 1,4-dioxane (0.2 mL) 4 M HCl in dioxane (3.22 mL, 12.9 mmol) was added and stirred at room temperature for 4 h. The reaction mixture was evaporated *in vacuo*, triturated with pentane and lyophilized from MeCN:H$_2$O to yield (1S,3S)-N^1-(5-(pentan-3-yl)pyrazolo[1,5-a] pyrimidin-7-yl)cyclopentane-1,3-diamine hydrochloride (0.9 g, 2.5 mmol, 97% yield) as a pale-yellow sticky solid. The reaction mixture was monitored by TLC (100% EtOAc, Product R$_f$ = 0.1, SM R$_f$ = 0.8). **^{1}H NMR** (400 MHz, DMSO-d_6) δ 15.00 (s, 1H), 9.93–9.86 (m, 1H), 8.51 (s, 3H), 8.30 (s, 1H), 6.84 (s, 1H), 6.58 (s, 1H), 4.95 (q, J = 7.8 Hz, 1H), 3.77–3.66 (m, 1H), 2.84–2.71 (m, 1H), 2.29–2.05 (m, 4H), 1.94–1.63 (m, 6H), 0.81 (t, J = 7.4 Hz, 6H). ^{13}**C NMR** (100 MHz, DMSO-d_6) δ 161.23, 148.95, 145.40, 139.54, 91.18, 85.59, 52.49, 49.15, 47.47, 38.80, 29.85, 28.96, 26.77, 11.70. **LC-MS** (m/z 287.21, found 288.0 [M+H$^+$]) *(1S,3S)-N^1-(5-(pentan-3-yl)pyrazolo[1,5-a]pyrimidin-7-yl)cyclopentane-1,3-diamine (KB-0742).*

KB-0742
(free base)

To (1S,3S)-N^1-(5-(pentan-3-yl)pyrazolo[1,5-a]pyrimidin-7-yl)cyclopentane-1,3-diamine hydrochloride (0.2 g, 0.56 mmol) aqueous NH$_3$ (4.0 mL, 0.56 mmol) was added and the resulting reaction mixture stirred at rt for 4 h. The reaction mixture was evaporated *in vacuo*, triturated with pentane and lyophilized from MeCN:H$_2$O to give (1S,3S)-N^1-(5-(pentan-3-yl)pyrazolo[1,5-a]pyrimidin-7-yl)cy-clopentane-1,3-diamine (140 mg, 0.49 mmol, 87.8% yield) as a pale-yellow sticky solid. The reaction mixture was monitored by TLC (100% EtOAc, Product R$_f$ = 0.1, SM R$_f$ = 0.1). **^{1}H NMR** (400 MHz, DMSO-d_6) δ 7.95 (d, J = 2.2 Hz, 1H), 6.86 (s, 1H), 6.29 (d, J = 2.2 Hz, 1H), 5.95 (s, 1H), 4.31–4.19 (m, 1H), 3.57–3.44 (m, 1H), 2.52–2.44 (m, 1H), 2.36–2.22 (m, 1H), 2.09–1.79 (m, 3H), 1.80–1.59 (m, 5H), 1.58–1.24 (m, 3H), 0.83 (t, J = 7.4 Hz, 6H). ^{13}**C NMR** (100 MHz, DMSO-d_6) δ 165.12, 148.82, 145.89, 142.90, 93.65, 84.85, 51.50, 50.99, 50.92, 41.74, 34.00, 30.53, 27.27, 11.98. **LC-MS** (m/z 287.21, found 288.5 [M+H$^+$])

QUANTIFICATION AND STATISTICAL ANALYSIS

For relevant experiments, number of replicates, error bars, statistical test, and P values are noted in the respective figure legends and in the corresponding experimental methods sections.